Materials & Design 219 (2022) 110811

Contents lists available at ScienceDirect

Materials & Design

journal homepage: www.elsevier.com/locate/matdes

Hybrid coatings for orthopaedic implants formed by physical vapour deposition and microarc oxidation

Roman Gabor [a], Ladislav Cvrček [b], Martina Doubková [c,d], Václav Nehasil [e], Josef Hlinka [f,g], Petr Unucka [h], Matěj Buřil [b], Adéla Podepřelová [g], Jana Seidlerová [a], Lucie Bačáková [c]

[a] Nanotechnology Centre, CEET, VSB – Technical University of Ostrava, 17, listopadu 15/2172, 708 00 Ostrava-Poruba, Czech Republic
[b] Department of Materials Engineering, Faculty of Mechanical Engineering, Czech Technical University in Prague, Karlovo náměstí 293/13, 120 00 Prague 2, Czech Republic
[c] Laboratory of Biomaterials and Tissue Engineering, Institute of Physiology of the Czech Academy of Sciences, v.v.i., Videnska 1083, 142 20 Prague 4, Czech Republic
[d] Charles University, Second Faculty of Medicine, V Uvalu 84, 150 06 Prague 5, Czech Republic
[e] Department of Surface and Plasma Science, Charles University, Prague, Czech Republic
[f] Department of Materials Engineering, Faculty of Materials and Technology, VSB-Technical University of Ostrava, 17, listopadu 2172/15, 708 00 Ostrava-Poruba, Czech Republic
[g] Centre for Advanced Innovation Technologies, VSB-Technical University of Ostrava, 17, listopadu 2172/15, 708 00 Ostrava-Poruba, Czech Republic
[h] VUHZ, a.s., 739 51 Dobra, Czech Republic

HIGHLIGHTS

- Unique combination of PVD and MAO techniques was used to prepare hybrid coatings to improve Ti-6Al-4V alloy properties.
- Prepared hybrid coatings with ZrTi exhibited improved corrosion and abrasion resistance, and a lower coefficient of friction.
- Hydrophilic oxide structure of prepared hybrid coatings increased osteogenic differentiation of human bone marrow mesenchymal stem cells *in vitro*.
- Combined use of MAO nad PVD techniques provides new possibilities of fine tuning the material surface layer properties.

GRAPHICAL ABSTRACT

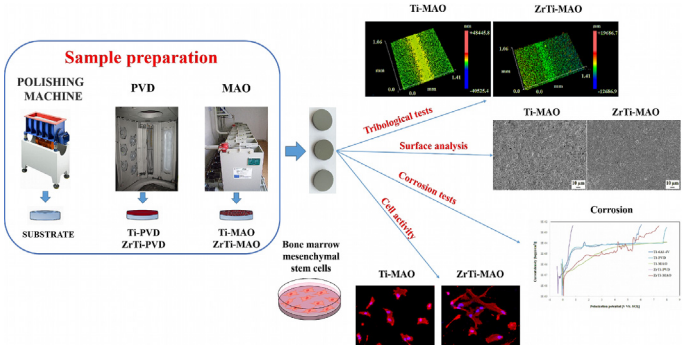

ARTICLE INFO

Article history:
Received 14 December 2021
Revised 29 May 2022
Accepted 31 May 2022
Available online 3 June 2022

Keywords:
Ti-6Al-4V
PVD coating
MAO process
Corrosion protection
Tribology
Mesenchymal stem cells

ABSTRACT

This study is focused on the preparation of new hybrid layers intended for surface modification of Ti-6Al-4V alloys for potential orthopaedic and dental applications. Combination of the technology of physical vapour deposition (PVD) and subsequent micro-arc oxidation (MAO) was utilized for the deposition of Ti and ZrTi to form hybrid oxide layers. The oxide layers were prepared using an alkaline electrolyte with glycerol as an additive under micro-arc discharge conditions with different Si content on their surfaces. The hybrid ZrTi coatings with a Zr/Si structure achieved the best tribological properties described by a low friction coefficient of 0.3 and high abrasion resistance. There was also an increase in corrosion potential and polarization resistance of hybrid ZrTi coatings. Although the proliferation of human bone marrow mesenchymal stem cells was slower on these hydrophilic Ti and ZrTi coatings than both on uncoated Ti-6Al-4V and the reference tissue culture polystyrene dishes, both types of hybrid coating promoted greater osteogenic differentiation of these cells, indicated by approx. twice as high activity of alkaline phosphatase. The hybrid oxide layers newly developed in this study – especially the layers with Zr – are therefore promising for coating metallic bone implants.

https://doi.org/10.1016/j.matdes.2022.110811
0264-1275/

1. Introduction

The design and the uses of biomaterials for bone implantation are closely bound to their strength, modulus of elasticity, wear resistance and non-toxicity, osseointegration or bioinertness. High osseointegration potential, i.e. attractiveness for the adhesion, growth and phenotypic maturation of bone cells, is needed for long-term/permanent orthopedic implants, such as stems for replacements of large and small joints (e.g., hip, knee, shoulder, and trapeziometacarpal joints) and for stomatological implants, especially for parts which are integrated into the bone (e.g., the stems and cups of hip joint replacements). Firm osseointegration of these implants improves their stability, prolongs their lifetime and, at the same time, reduces the likelihood of failure and the need for reoperation. Bioinertness, i.e. repulsiveness of a biocompatible material for cell adhesion and growth, is needed for short-term/temporary implants, e.g. for traumatological implants such as splints, wires, screws or spikes, so that they can be removed easily after the bone damage has healed [1].

The excellent corrosive and mechanical properties of pure Ti and Ti alloys make them suitable for application in both types of bone implants mentioned above [2]. Significantly better mechanical properties were achieved via stabilisation of the $\alpha + \beta$ phases in Ti-6Al-4V alloy [3]. Titanium alloys with a stabilised β phase, containing elements such as Nb, Ta or Zr, are becoming more and more popular. The main benefits of these alloys are their lower modulus of elasticity and the absence of toxic elements such as Al and V [1]. Growing evidence of the release of these elements into the body is being gathered. This release is linked with neurodegenerative diseases like Alzheimer and Parkinson, peripheral neuropathy, and also can affect negatively the proliferation of adjacent bone cells, extracellular matrix synthesis and the formation of bone apatite, which an lead to osteomalacia [4]. The cytotoxicity of these elements is further potentiated or enhanced by the release of other metal ion species (particularly Ti), which is of increasing importance, especially during tribocorrosion phenomena. This type of synergistic adverse effect of the released ions is well-known both for pure Ti and for titanium alloys, and it is therefore crucial to address the material surface degradation process in the human body [5]. Titanium itself in the form of ions, and in the form of nanoparticles and microparticles, can cause cytotoxic, inflammatory, allergenic and even mutagenic and carcinogenic effects [6].

The well-known poor tribological properties of Ti and titanium alloys, accompanied by a high friction coefficient and insufficient abrasion resistance, place increased emphasis on the subsequent surface treatment ensuring sufficient tribological, corrosion, and biocompatible properties [7]. Commercial coatings for implants that are most commonly applied to improve these properties include diamond-like carbon (DLC) [8], nitride [9] and oxide ceramic coatings [10]. Other promising bioactive coatings include various inorganic substances, such as calcium phosphates or bioactive glass, and also organic substances, such as natural polymers (collagen, gelatin, cellulose, chitosan, alginate, hyaluronic acid) and synthetic polymers (polycaprolactone, polyether ether ketone, poly-L-lactic acid, poly lactic-co-glycolic acid, polyurethane, polyvinyl alcohol), which can serve as carrier matrices for the delivery of therapeutic drugs, antimicrobial agents, growth factors and other biologically active compounds [11].

Steady progress in the application of protective coatings in the last two decades has achieved required properties such as wear resistance, good tribological properties, oxidation resistance, corrosion resistance, and a low coefficient of friction [12]. Coatings providing these properties can be applied using physical vapour deposition (PVD) technology [13], for example cathodic arc evaporation (CAE), direct current (DC) or pulsed DC magnetron sputtering [14], radio frequency (RF) magnetron sputtering [15], and high power impulse magnetron sputtering (HIPIMS), which is widely applied today [16]. Other important coating technologies include chemical vapor deposition (CVD), electrophoretic deposition, sol–gel deposition, layer-by-layer deposition, biomimetic deposition, dip coating, drop coating, plasma spraying and 3D printing [11].

A promising alternative to the methods mentioned above, microarc oxidation (MAO), also referred to as the plasma electrolytic oxidation (PEO) technique, can be used to prepare continuous ceramic oxide layers with excellently high adhesion to the substrate (e.g. Ti, Al, Nb, Zr, Ta, Hf), and with high resistance to wear and corrosion. In the preparation of hard ceramic layers, a pulsed BI- or UNI-polar mode is used to produce the discharge observed during plasma electrolysis in a liquid electrolyte [10]. The oxide layer prepared by the MAO technique consists of a porous amorphous outer layer and a compact crystalline inner layer [17]. The growth of the ceramic layer (up to 20 μm) occurs at temperatures of 10^3-10^4 K and at a pressure of 10^2-10^3 Pa after exceeding the breakdown voltage while the formation of plasma channels with a micro-arc discharge is taking place [18]. The surface properties of these ceramic layers, including their porosity, roughness, and chemical composition, determine whether their successful application range is for short-term implants or for long-term implants [19]. The properties of ceramic coatings defined in this way are affected not only by the applied voltage, the pulse size, the pulse width and the process time but also by the composition of the electrolyte that is applied. The ions (Ca, P, Si) from the electrolyte are incorporated into the coating and affect its functional properties, including corrosion resistance, abrasion resistance, and biocompatibility [20]. The roughness and the porous structure of the outer porous layer of the MAO coating negatively affect the resulting coefficient of friction [21]. Although MAO coatings achieve high corrosion resistance, both layer failure and reduced corrosion resistance can occur under loading. In an effort to eliminate these shortcomings, many authors have investigated the possibility of doping the MAO electrolyte using nano particles TiO_2 [22], MoS_2 [23], ZrO_2 [24] or yttrium [25] and the use of secondary layer deposition in the form of DLC coating or graphene coating [26]. The Al/Ti-6Al-4V duplex system prepared by a combination of MAO and magnetron sputtering was also tested with the aim to improve the tribological properties of the MAO coatings [27]. The options available in the use of the hybrid system preparation technique allow a more detailed study of the PVD-deposited layer and its final properties, achieved by subsequent MAO. Application of this procedure makes it possible, using PVD with the required functional properties, to enrich the MAO layers with the oxides of deposited metals that are formed. To increase the osteointegration properties, porous Ca/P layers on Ti-6Al-4V and Ti-29Nb-xHf substrates were prepared using a combination of MAO/PVD techniques [28]. Subsequently, the RF magnetron sputtering technique was used on the prepared MAO porous layer for the deposition of an Mn layer [29], and a Zn layer [30].

Several works [31,32] have studied titanium alloys with Nb, Zr, Ta, which – after MAO treatment – achieved increased wear resistance and excellent corrosion properties due to the presence of stable oxides (e.g. Ta_2O_5, $ZrTiO_4$).

Due to their high corrosion resistance, very good mechanical properties and excellent biocompatibility, zirconium and its alloys are promising biomaterials for orthopaedic implants [33]. MAO applications - previously used for titanium and its alloys - can also be used for the preparation of oxide layers based on zirconium [34]. The zirconium oxide layers thus prepared can increase corrosion resistance and wear resistance, and can reduce the coefficient

of friction [35], while eliminating the release of toxic Al and V ions from the Ti-6Al-4V alloy substrate.

As proved by our earlier study [36], MAO enables the preparation of highly hydrophilic and bioinert surfaces that reduce cell adhesion and growth without affecting the cell viability, and further modification of the MAO-deposited layers can modulate the surface wettability and attractiveness for cell colonisation in a controllable manner.

Options for readily modifying the process parameters of the formation and composition of a material coating are valuable for fine tuning the surface properties to modulate the desired cell response. For this purpose, we propose the application of a novel combination of surface treatment and deposition techniques of magnetron sputtering and MAO. Although each of these techniques is commonly used for modifying materials, they have not yet been systematically used and researched together. The combined use of these techniques could provide an interesting opportunity to study their possibilities with regard to their material properties and their performance in biological environments represented by cultures of osteogenic cells *in vitro*. In this study, a combined PVD and MAO technology was used for the development of Ti and ZrTi layers on a Ti-6Al-4V substrate. These layers were then characterized in terms of their physical, chemical and tribological properties and their interaction with human bone marrow mesenchymal stem cells in cultures on their surface. We found that the deposition of both types of coatings, particularly ZrTi, improved the resistance of the samples against friction, wear and corrosion, and improved the cell osteogenic differentiation.

2. Materials and methods

2.1. Sample preparation

Round samples of Ti-6Al-4V titanium alloy (15 mm diameter, 2.6 mm thickness) were subjected to mass finishing to unify the surface using an HV 20 vibratory finishing machine (OTEC, Germany) for 8 h with the use of KF 10 plastic bodies. Ti and ZrTi PVD layers were deposited on mechanically treated samples of Ti-6Al-4V alloy in the Hauzer Flexicoat 850 (Hauzer, Netherlands) PVD unit based on cathodic arc evaporation. The targets used for arc evaporation of Ti and ZrTi were 63 mm in diameter, and the pressure in the working chamber was 10^{-3} mbar during the application. The process parameters of the PVD unit used for deposition of the Ti and ZrTi layers are given in Table 1.

Samples with PVD layers (Ti-PVD, ZrTi-PVD) deposited on a Ti-6Al-4V substrate were modified under MAO conditions using a pulse source at 93 Hz, 7 % duty cycle, voltage 500 V reached in 30 s, voltage 500 V for 15 min (Fig. 1). Samples with MAO coatings (Ti-MAO, ZrTi-MAO) were prepared in an electrolyte containing 15 g/L Na_2SiO_3 $9H_2O$; 8 g/L NaOH; 80 g/L glycerol (conductivity 28.8 mS/cm, pH 12.5).

Table 1
Process parameters.

Parameters	Ti	ZrTi
Target	99.98 % Ti	85 % Zr / 15 % Ti
Coating pressure (mbar)	5.0 10^{-3}	8.0 10^{-3}
Temperature (°C)	430	430
Gas	Ar	Ar
Gas Flow (sccm)	540	380
Deposition time (min)	180	150
Current on target (A)	60	80
Voltage bias (V)	−80	−80

2.2. Surface analysis of the coatings

The surfaces and cross-sections of the coatings were studied using the JEOL JSM-7610F Plus (JEOL, Japan) Scanning Electron Microscope (SEM) equipped with an autoemission cathode as the electron source. The samples were scanned in BSE mode (20 keV accelerating voltage) with detection of the secondary electrons. The chemical composition of the coating was determined using an energy dispersive X-ray spectrometer (EDX, Oxford Instruments). The KSG 110 Calotest device (INOVAP, Germany) was used to determine the thickness of the PVD coatings. The MAO coating thickness was studied by SEM from polished cross-sections in back scatter emission mode. An atomic force microscope (AFM, LiteScope^{TM}) was used in semi-contact mode to measure the topography and the surface roughness of the sample surfaces. The correlative analysis also provides data from both AFM and SEM and allows a 3D correlative probe and electron microscopy view (CPEM, Nenovision s.r.o.). Surface roughness R_a measurements (the arithmetic average of the absolute values of the profile heights), R_t measurements (the vertical distance between the highest and lowest points of the profile) and R_z measurements (the maximum height of the profile) were carried out in contact mode by AFM (AFM LiteScope^{TM}).

The chemical states and the composition of the prepared layers were analysed using the method of photoelectron spectroscopy - XPS (X-ray photoelectron spectroscopy), which was carried out in an ultra-vacuum apparatus with a basic pressure of 1.10^{-7} Pa. Photoelectrons were emitted using an X-ray tube with a double anode (Al, Mg). The Al $K\alpha_{1,2}$ line with primary energy of 1486.6 eV was used in the experiments. XPS spectra were recorded using an Omicron EA125 hemispherical analyser.

2.3. Tribological and adhesion tests

The friction coefficient and the wear rate were tested using a CSM THT pin-on-disc tribometer (CSM Instruments, Switzerland). The friction pair consisted of the tested planar sample and an Al_2O_3 ball 6 mm in diameter. The tests were performed at room temperature in phosphate-buffered saline (PBS), which served as a simulation of the human body environment. The solution was prepared by dissolving one PBS tablet (Sigma-Aldrich, USA) in 200 mL of distilled water. The solution contained 10 mM phosphate buffer, 2.7 mM KCl and 137.0 mM NaCl with pH 7.4 at 25 °C.

During the tribological test, a normal load of 1 N, linear sliding speed 50 mm s^{-1} and number of laps 5000 with a radius of 6 mm were used. Each measurement was repeated twice for each sample. The coefficient of friction (μ) was calculated from the ratio of the tangential friction force and the normal force. The wear of the surface of the Al_2O_3 ball and the width of the wear track on the planar sample were analysed using an Olympus DSX1000 (Olympus Corporation, Japan) digital microscope after the test. The wear rate was calculated from the following equation (Archard,1953):

$$k = V / F\,s$$

where k is the wear rate, V is the wear volume, F is the normal load, and s is the sliding distance. The wear volume was obtained by multiplying the area of the wear track cross-section and the circumference of the wear track. The wear track cross-section area was calculated from the wear track profile, which was analysed by a Zygo NewView 7200 optical profilometer (Zygo Corporation, USA).

The CSM Revetest Xpress+ (CSM Instruments, Switzerland) scratch tester was used for adhesion evalution. The scratch tester was equipped with a Rockwell diamond indenter (tip radius 200 μm). The scratch test load was set to increase linearly from

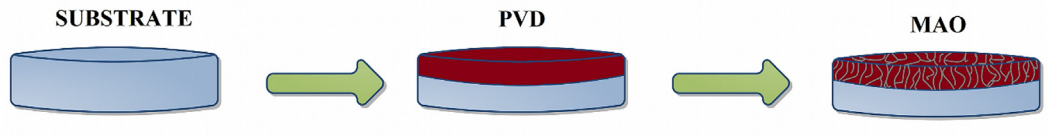

Fig. 1. Schematic diagram of the deposition and layer modification process applied to the Ti-6Al-4V substrate material.

1 N to 30 N along the 5 mm scratch path with linear speed 10 mm. min^{-1}.

2.4. Corrosion tests

As the corrosion resistance of titanium and its alloys is significant, direct exposure corrosion tests would not be suitable; a potentiodynamic polarisation method was therefore used for determining the corrosion parameters of the tested samples. All electrochemical tests were performed using a Voltalab PGZ 100 potentiostat equipped with Voltamaster 10 software. The parameters of the test were used according to the ASTM F 2129 and ASTM F 746 standard test methods [37]. PTFE/PE corrosion cells with a lower exposure hole (0.5 cm^2) and a volume of 20 mL were used for testing. The samples were tested in an isotonic physiological solution (0.9 wt% NaCl in double-distilled H_2O) in order to simulate the environment of a living tissue. No gas bubbling was applied during testing, and the temperature was set to 25 °C. A three-electrode setup was used, consisting of a sample connected as a working electrode, a saturated Calomel electrode (SCE, +241 mV vs SHE) set as a reference electrode, and a high purity carbon rod connected as an auxiliary electrode.

A 60-minute time lag was applied after filling the corrosion cells with the solution to stabilise partial corrosion processes. After the time gap, an electrochemical impedance spectroscopy (EIS) method was used to determine the electrochemical parameters of the tested surface layers. Before starting the potentiodynamic polarisation, the initial potential value was set to −70 mV vs. the open circuit potential (OCP) after stabilisation of the corrosion equilibrium, with the polarisation rate set to 60 $mV.min^{-1}$. The dependence between the current flowing through the sample and the potential applied to the test sample was recorded during the measurement. The potential was gradually applied to the tested sample, which increased over time with the value of the polarisation rate.

2.5. Contact angle

The angle between the tested surface and the physiological solution was evaluated by the sessile drop method. The surface contact angle was measured by the SEE system, and the free surface energy was calculated by Advex Instrument software (Advex Instruments, s.r.o., Czech Republic). Two μL droplets of high purity water were applied to the tested surface, and the contact angle θ was determined by the tangent to the drop profile at the point of contact of the three phases (liquid, solid and gas) with the line of the surface of the sample.

2.6. Cell culture conditions

Human mesenchymal stem cells derived from bone marrow (hMSCs; No. 7500, ScienCell Research Laboratories, USA) were used in all experiments. Prior to the experiments, the hMSCs were cultured in 75 cm^2 tissue culture flasks (TPP, Switzerland) in 15 mL of Mesenchymal Stem Cell Medium (MSCM medium; No.7501, ScienCell Research Laboratories, USA) to reach ca 70% confluence. The Ti-6Al-4V samples (Ti-6Al-4V, Ti-MAO, ZrTi-MAO) were disinfected with ethanol for 2 h, were rinsed in dH_2O, were sterilised in an autoclave, and were then inserted into tissue culture polystyrene 24-well plates (TPP, Switzerland). The hMSCs were seeded on these samples at a density of 9,000 viable cells per well (ca 5,000 cells/cm^2) in 1.5 mL of α-MEM medium (No. 11900-016, Gibco, USA) supplemented with 10% of fetal bovine serum (FBS), L-glutamine (2 mmol/L; No. A2916801, Gibco, USA) and gentamicin (40 μg/mL). In addition to the samples, the cells were also seeded directly into the tissue culture plate wells (PS), to provide information about the standard cell behaviour. The cells were cultured at 37 °C in a humidified atmosphere with 5% CO_2 for 14 days. In order to support osteogenic differentiation of the cells, the culture medium was enriched with ascorbic acid (50 μmol/L; No. 49752-10G, Sigma-Aldrich, USA), β-glycerophosphate (20 mmol/L; No. G9422, Sigma-Aldrich) and dexamethasone (10 nmol/L; No. D2915, Sigma-Aldrich). The medium was replaced twice per week.

2.7. Fluorescence staining

Fluorescence staining was used for visualising and analysing the cell spreading area and morphology (day1), and for evaluating the number and the viability of the cells growing on the samples (day 1, 3, 7 and 14). The samples were rinsed with PBS, then fixed with 4% paraformaldehyde (pH 7.4, 15 min), and were rinsed again twice with PBS. The fixed samples were treated with 1% bovine serum albumin in PBS containing 0.1% Triton X-100 (20 min) and with 1% Tween 20 in PBS (20 min) (both Sigma-Aldrich, USA). Subsequently, the cell nuclei were stained with DAPI (100 ng/mL, blue fluorescent signal; No. 32670, Sigma-Aldrich), the cell membrane and cytoplasm were stained with Texas Red C_2-maleimide (20 ng/mL, red fluorescent signal; Molecular Probes, Invitrogen, USA), or the F-actin cytoskeleton was stained with TRITC-conjugated phalloidin (100 ng/mL, red fluorescent signal; Sigma-Aldrich). All dyes were diluted in PBS and were added to the cells for 1 h at room temperature (protected from light).

A parallel set of samples for each time interval was rinsed with PBS and was stained with a Live/Dead Viability/Cytotoxicity kit for mammalian cells (No. L3224, ThermoFisher Scientific, USA) according to the manufacturer's instructions. Calcein AM stains the living cells in green, whereas ethidium homodimer 1 stains the dead cells with damaged cell membranes in red. Additional staining of the cell nuclei with DAPI was performed on day 7 and 14 for easier cell counting.

Microphotographs (20 per samples/well) of randomly chosen fields were taken with an Olympus IX51 epifluorescence microscope, equipped with a DP70 camera (both from Olympus Corp., Japan). The microphotographs were analysed in ImageJ FIJI software (https://imagej.net/Fiji; 51). The initial cell spreading areas are presented in μm^2. The cell viability was determined as the percentage of living cells on the sample. The cell population densities on the samples are presented as the cell number per cm^2 on a log scale to assess proliferation. The data from day 1 and day 3 were used for calculating the cell population doubling times, according to the following equation:

$$DT = log2\frac{t - t_0}{logN_t - logN_{t_0}}$$

The time intervals are represented by t_0 (day 1) and t (day 3), and Nt_0 and Nt represent the number of cells in a particular time interval.

2.8. Resazurin assay

A resazurin assay based on the activity of mitochondrial enzymes was used to investigate the metabolic activity of the hBMSC cells. On days 1, 3, 7 and 14 of cultivation, the samples were transferred to fresh 24-well culture plates with a fresh culture medium without phenol red supplemented with 10% of FBS. The samples were then incubated with resazurin (No. R7017, Sigma–Aldrich, USA) diluted to a final concentration of 40 μmol/L in a fresh culture medium without phenol red (1 mL/well) at 37 °C in a humidified atmosphere containing 5% CO_2, protected from light. After 4 h (day 1 and 3) or 2.5 h (day 7 and 14) of incubation, the fluorescence was measured (Ex/Em = 530/590 nm) by a Synergy HT Multi-Mode Microplate reader (BioTek, USA) in triplicate aliquots. A solution incubated in a well without cells served as a blank control. The results were corrected to the background control (solution without cells) and were then relativised to the estimated total number of cells growing on each sample.

2.9. ALP assay

A quantitative analysis of alkaline phosphatase (ALP) enzymatic activity to assess early osteogenic differentiation of the cells on the samples was performed using 1-Step PNPP Substrate Solution (p-nitrophenyl phosphate; No. 37621, ThermoFisher Scientific) on days 7 and 14 of culture. The samples were rinsed with PBS three times. After a total of 250 μL of PNPP had been added to each sample, the culture plate was incubated for 20 min at room temperature for the reaction to develop. The absorbance of the water-soluble yellow-colour product was measured at 405 nm using a Synergy HT Multi-Mode Microplate reader (BioTek, USA), in duplicates for each well. The absorbance results were corrected to a blank control (PNPP solution without cells), and were then relativised to the estimated total number of cells growing on each sample.

2.10. Statistical analysis

All biological experiments were performed independently three times with samples in triplicate in each time interval (n = 3 for each experimental group). Statistical analyses and data visualization were performed in GraphPad Prism 8.3.0 (GraphPad Software, USA). One Way ANOVA with Tukey's test or Kruskal-Wallis ANOVA with Dunn's post hoc test were performed on the data from the biological experiments. The data are expressed in summary graphs as median with interquartile range (IQR). The results were considered statistically significant at $p < 0.05$.

3. Results and discussion

3.1. Morphology and chemical analysis

Fig. 2a-c presents SEM images of the surface structure of the substrate and of the PVD coating. The images confirm the homogeneous and compact structure of the coatings regarding their thickness and roughness, which was also determined by a Calotest instrument (Table 2). The results of the CPEM analysis, presented in Fig. 2d-f, revealed microscopic defects on the surfaces (such as traces of mechanical treatment or droplets). The occurrence of these defects following PVD deposition can be reduced by lowering the arc target current [38].

The SEM and CPEM images in Fig. 3a-d show that the surface morphology of the MAO coating is a compact porous structure with an average pore size of about 1 μm. The formation of a micro-arc discharge was recorded after reaching 500 V, and it was followed by a decrease in current associated with the growth of the oxide layer. The presence of commonly known structural microscopic defects of the MAO coating involving cracks was not confirmed on the studied surfaces with the unique CPEM technology. The development of the coating is accompanied by the formation of so-called volcanic craters (Fig. 3) during micro-discharges, when the released melt of the substrate (PVD layer) is deposited via discharge channels on the surface. Well-visible changes in surface topography imaged using CPEM technology indicate through 3D imaging the presence of craters that affect the resulting roughness of the hybrid MAO layers compared to the surface roughness for the deposited PVD layers (Fig. 2).

The resulting measured thickness and roughness parameters of the MAO coatings are given in Table 2. The layer thicknesses were determined from the cross-sections of individual MAO coatings on which the distribution of the elements present in the layer was evaluated. Figs. 4 and 5 show the presence of the outer and inner MAO layers. Element mapping from cross-sections of the Ti-MAO sample (Fig. 4) and of the ZrTi-MAO sample (Fig. 5) confirmed both the presence of elements from PVD deposition and the elements incorporated from the solution.

The resulting values of the porosity structure of the MAO coatings (Table 2) confirmed the increase in roughness in all three monitored parameters (R_a, R_z, R_t) of the surfaces of the MAO coatings in comparison with the bare substrate and the PVD coatings (Ti-PVD, ZrTi-PVD). The resulting surface structure is due to the high temperature (10^5-10^7 K/s) and the pressure in the discharge of the channels during the MAO process. The resulting melt passes through the discharge channel and, after leaving the channel, it solidifies in the electrolyte environment [18]. The growth of the surface roughness and of the oxide layer is mainly associated with the process conditions (voltage, current density, time, temperature, electrolyte composition) and the presence of additives. The effect of glycerol as an additive on the surface roughness and on the structure of the MAO coating was described in detail in an earlier study by Gabor *et al.* [39]. In an effort to reduce the surface roughness and to improve the tribological and corrosive properties of the coating, glycerol was used as an additive in this work.

The different values of the achieved thickness and roughness of the MAO coating (Table 2) are caused by the different development of the spark discharge, while the distribution and the intensity of the spark discharge directly affect both the resulting surface morphology and its phase composition [40]. The course of the MAO process is influenced by the different melting temperatures of Ti (1660 °C), Zr (1852 °C) and of ZrTi, which may lead to more difficult MAO development of the ZrTi-PVD sample, subsequently affecting the resulting surface microstructure [41]. The higher roughness parameters of the Ti-MAO coating are caused by the greater intensity and the larger amount of microdischarges on the surface of the sample than on the ZrTi-MAO coating. High microdischarge temperatures lead to dissolution of the substrates and to subsequent reactions with the electrolyte elements that are present, including rapid solidification and the formation of oxides that affect the resulting surface morphology [42].

Cross-sections and elemental mapping confirm the phenomenon of MAO coatings, the presence of a compact inner layer and a porous outer layer (Figs. 4 and 5). The outer layer is highly porous, rough, amorphous and not corrosion-resistant. The dense inner layer, characteristic of the MAO process, is corrosion-resistant, crystalline and its thickness increases with the process-

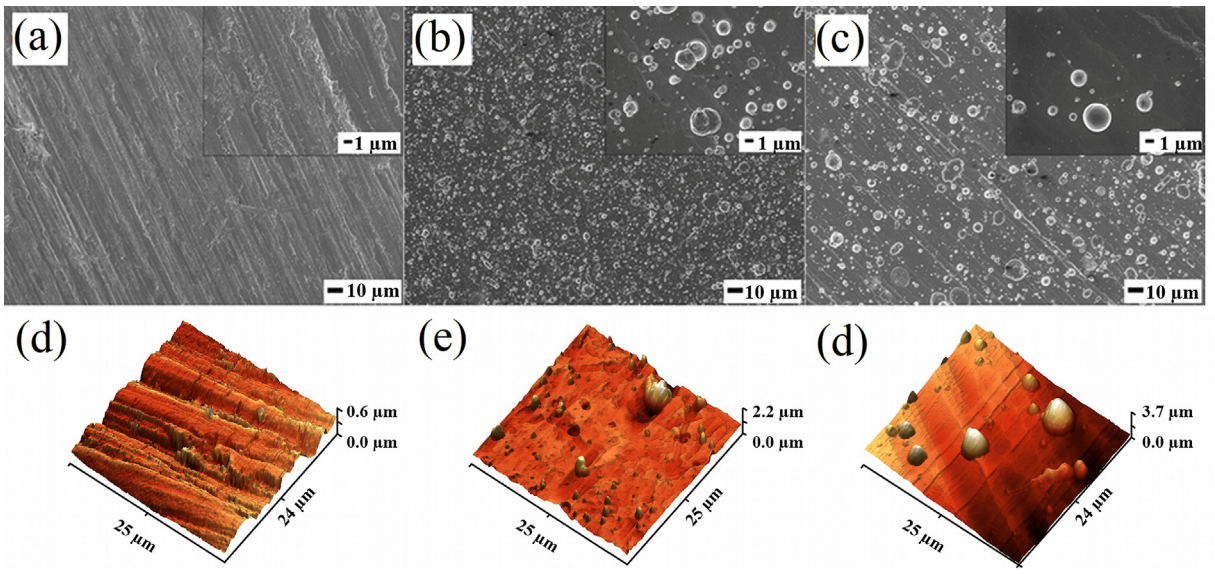

Fig. 2. Morphology of PVD coatings. SEM images of the Ti-6Al-4V substrate (a), Ti-PVD (b) and ZrTi-PVD (c); AFM images of the Ti-6Al-4V substrate (d), Ti-PVD (e) and ZrTi-PVD (f).

Table 2
Surface roughness and thickness of samples.

Sample	Roughness (µm)			MAO-coating (µm)		PVD-coating (µm)
	R_a	R_z	Rt	inner layer	outer layer	layer
Substrate	0.09 ± 0.02	0.31 ± 0.62	0.55 ± 0.10	–	–	–
Ti-PVD	0.19 ± 0.09	0.64 ± 0.30	1.23 ± 0.30	–	–	3.4 ± 0.50
ZrTi-PVD	0.24 ± 0.11	0.84 ± 0.38	1.55 ± 0.69	–	–	2.8 ± 0.44
Ti-MAO	0.82 ± 0.16	2.37 ± 0.40	3.86 ± 0.64	0.60 ± 0.12	3.35 ± 0.49	–
ZrTi-MAO	0.58 ± 0.22	1.66 ± 0.58	2.75 ± 0.84	0.94 ± 0.11	4.25 ± 0.35	–

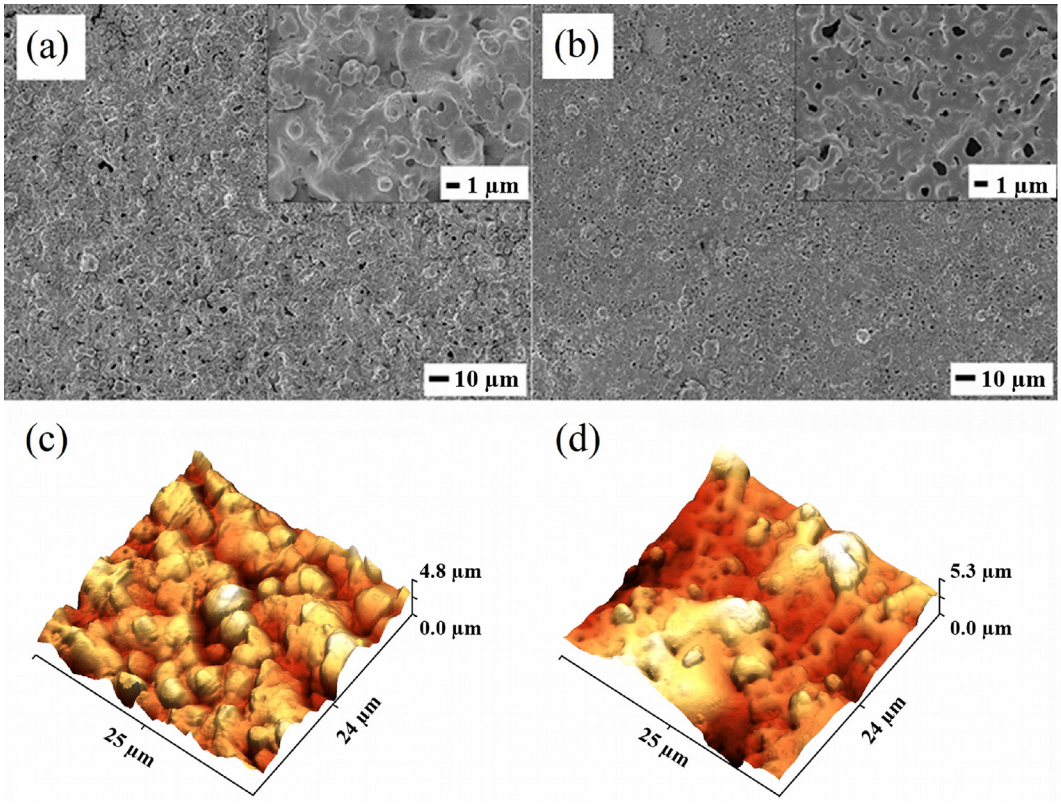

Fig. 3. Morphology of MAO coatings. SEM images of Ti-MAO (a) and ZrTi-MAO (b); AFM images of Ti-MAO (c) and ZrTi-MAO (d).

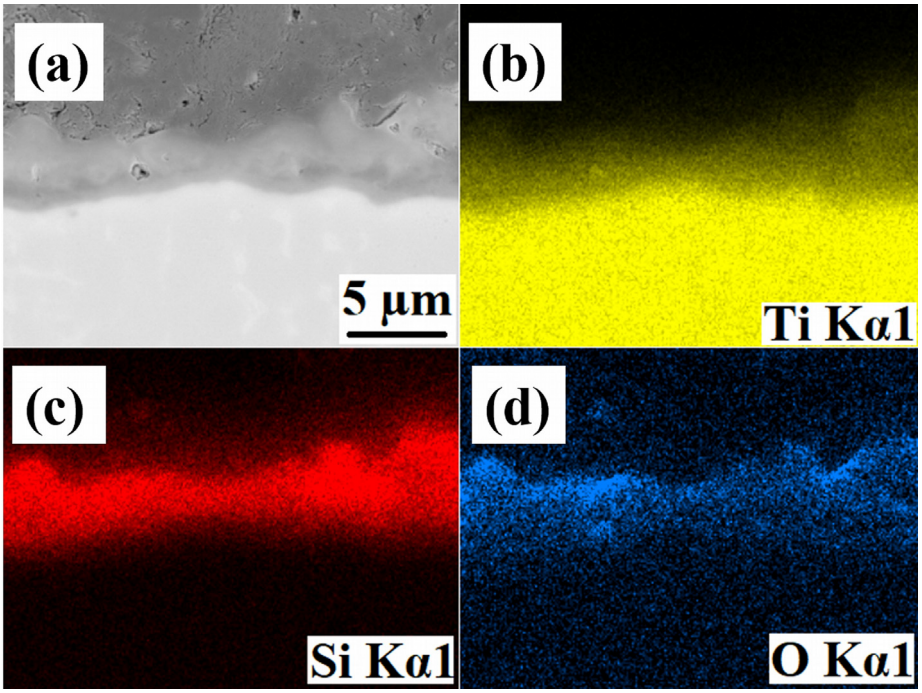

Fig. 4. Cross-section SEM images of the Ti-MAO coating (a) and elemental mappings of Ti, Si, O (b-d).

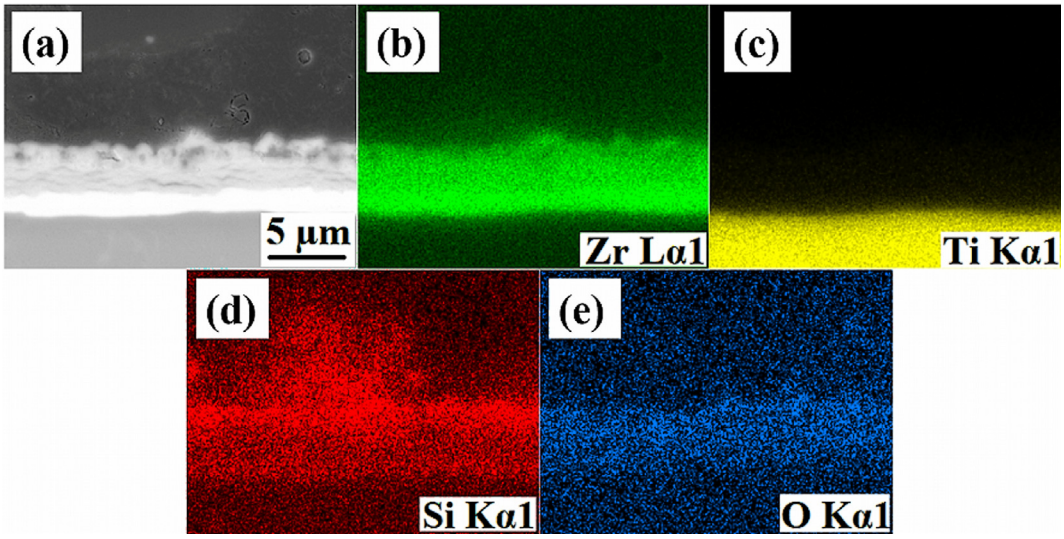

Fig. 5. Cross-section SEM images of the ZrTi-MAO coating (a) and elemental mappings of Zr, Ti, Si, O (b-e).

ing time [43]. The distribution of elements in the Ti-MAO coating is shown in Fig. 4, and EDX analysis confirmed the presence of Ti, Si and O elements (Table 3). Increased Si contents were determined mainly in the outer porous layer, according to Gabor *et al.* [36]. According to [44], the MAO process in alkaline conditions with the presence of silicates provides better wear resistance and corrosion resistance. The proportion of silicon in the coating volume differed significantly for MAO coatings - the ZrTi-MAO silicon content (Fig. 5) determined by EDX was lower in the coating volume (Table 3). On the contrary, the Si contents on the surfaces of the outer MAO layers about 20 nm in thickness were relatively close due to the sensitivity of the XPS method (Table 4). The reduction

Table 3
EDX results analysis of the Ti-MAO and ZrTi-MAO coatings.

Sample	Element (in at.%)			
	Ti	Si	Zr	O
Ti-MAO	9.4 ± 0.2	13.9 ± 0.2	–	76.7 ± 0.3
ZrTi-MAO	2.5 ± 0.1	3.2 ± 0.1	18.3 ± 0.6	76.0 ± 0.2

Table 4
XPS analysis results of MAO coatings.

Sample	Element (in at.%)					
	Ti	O	C	Si	Na	Zr
Ti-MAO	5.7	65.9	8.2	18.9	1.3	0.0
ZrTi-MAO	1.6	65.2	8.0	15.3	1.6	8.4

of the silicon content in the outer layer is probably associated with the migration of Zr ions towards the surface and the limited transfer of the silicon species from the electrolyte to the depth of the coating [45]. This fact is related to the development of so-called "soft" sparking, which is reflected in the high density of blue-white micro-discharges after the overall reduction of discharges over the entire sample area and noise reduction [46]. The resulting "soft" sparking is probably related to the occurrence of small diameter discharge channels and the associated limited mass transfer and reduced silicon content in the volume of the outer porous layer [47].

Both the composition of the surface and its chemical state were monitored by the XPS method. The results of the semi-quantitative analysis determined by the XPS method on individual samples (Ti-MAO, ZrTi-MAO) are shown in Table 4. The contents of the individual elements were determined from the peak area by the method of relative sensitivity factors after subtracting the Shirley background. The presence of Ti, O, C, Si and Na was registered on the surface of both samples. The presence of Zr from PVD deposition (ZrTi) was also determined on the surface of the ZrTi-MAO sample. Elements Si, Na and C were incorporated into the surface of the MAO layer of the electrolyte.

The chemical state of individual elements was determined from the peak shifts of individual elements. The axis of binding energies – E_B – was calibrated under the assumption that the main component of the peak C 1s lies at E_B = 282.5 eV and corresponds to the Si-C bond [48]. A second component was also determined at peak C 1s (Fig. 6), which has an intensity of approximately 15% of the total signal C and lies at E_B = 285.7 eV. According to Wang *et al.* [48], this binding energy corresponds to the C-O groups. On the surface of the Ti-MAO sample, two components of the Si 2p peak at E_B = 99.7 and 101.0 eV were detected. According to Wang *et al.* [49], this corresponds to the structure of Si-C and C-O-Si. On the ZrTi-MAO coating, three components of the Si 2p peak were registered, namely E_B = 97.7, 98.7 and 100.00 eV. There is probably an interaction of Si with Zr (Fig. 6), which is evident from the shift of E_B to lower values by approximately 1 eV. The peaks at E_B = 98.7 and 100.0 eV can both be identified as for the Ti-MAO sample, and correspond to Si-C and C-O-Si structures. The spectrum also has a peak at E_B = 97.7 eV. This value is comparable to E_B = 99.3 eV, reported in a study by Ding *et al.* [50] for the Zr-Si structure.

The overall structure of Si can be shifted to E_B lower by 1 eV. This peak can also be attributed to the Si-Si structure. Shifts of the Si 2p peaks to lower binding energies can be caused by a charge transfer from Zr to Si and other elements, because Zr has lower electronegativity (Pauling electronegativity 1.33) than Si (1.90) and other elements. This causes a reduction in the measured binding energy of the element to which the charge shifts moves. The O 1s oxygen peak (Fig. 6) of the Ti-MAO sample surface is wide, and can be divided into two components at energies of 529.3 and 529.9 eV. On the surface of the ZrTi-MAO coating, another component at E_B = 527.7 eV was identified. All these peaks can be explained by an oxidic bond, because the range of oxygen binding energies in oxides is relatively wide (528.1 – 531.1 eV) [51]. These are probably therefore oxides of Si, Ti and Zr. The Ti 2p peak on the Ti-MAO sample lies at E_B = 456.9 eV. Due to the energy distance of the Ti $2p_{3/2}$ and O 1s peaks of 72.8 eV, we conclude that Ti_2O_3 is present [52].

In both samples (Ti-MAO, ZrTi-MAO), the extension of the Ti 2p and O 1s spectra is evident. This suggests the presence of a mixture of lower Ti oxides and, at the same time, it corresponds to the measured O 1s binding energies. In the spectrum of zirconium Zr $3d_{5/2}$ (Fig. 6) on the surface of the ZrTi-MAO sample, we find two components at E_B = 177.6 and 179.2 eV. The peaks are widespread and the saddle between components $3d_{5/2}$ and $3d_{3/2}$ is almost

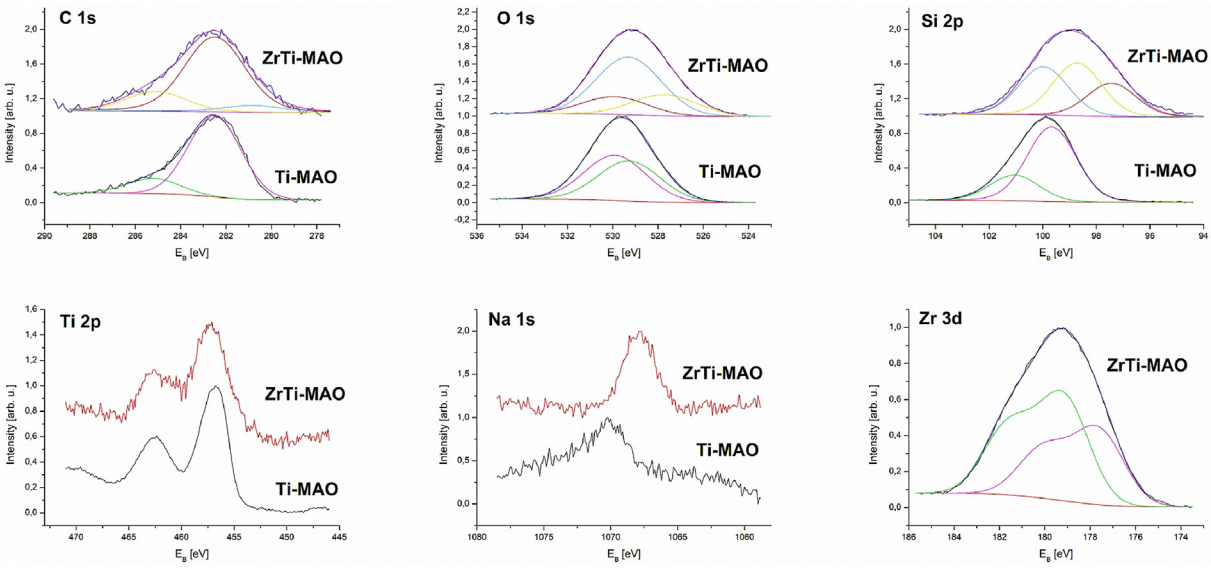

Fig. 6. XPS spectra of MAO coatings.

indistinguishable, indicating high dispersion of the Zr present in the layer. According to Ding *et al.* [50], who studied the effect of $ZrSi_2$ particles on phenol degradation, the determined binding energy E_B = 179.2 eV corresponds to the Zr/Si structure. The component with a lower binding energy E_B = 177.6 eV could not be identified according to the spectrum atlas [51]. The XPS spectrum of Zr $3d_{3/2}$ and Zr $3d_{5/2}$ of the ZrTi-MAO sample is probably influenced by the atomic dispersion of zirconium and/or by the change in the coordination number of zirconia to form a complex oxide phase, which appears to occur on the sample surface [53]. The Zr $3d_{5/2}$ binding energy values that were determined are lower than for pure ZrO_2 (182.5 eV). The Na 1 s peak at 1070.2 and 1067.9 eV binding energies was also registered on the surfaces of the sample (Ti-MAO, ZrTi-MAO).

The wettability of the surfaces was evaluated using the determined contact angles (CA) of the substrate and of the MAO coatings (Supplementary Fig. S1). Compared to the substrate, which had CA = 89.07° ± 3.28, the determined CA of the modified MAO coatings showed hydrophilic properties corresponding to CA = 72.32° ± 4.15 of the Ti-MAO coating and CA = 69.01° ± 5.63 of the ZrTi-MAO coating. The results confirm the well-known fact that MAO coatings, with their porous structure and greater roughness, are more hydrophilic than unmodified substrates [54].

3.2. Wear behavior and coating adhesion

The course of the coefficient of friction was first tested on the Ti-6Al-4V base material without surface treatment. Subsequently, this was compared with the course of the coefficient of friction for samples with a coating of pure Ti-PVD and ZrTi-PVD without and with MAO treatment. Fig. 7 shows that, after running-in, the coefficient of friction for the MAO samples is very stable, and that adhesive friction predominates. In the base material and in pure Ti and ZrTi metals, however. the course of the coefficient of friction is less stable, and a combination of adhesive and abrasive friction prevails. The average coefficient of friction of the tested samples is very similar, and ranges from 0.4 to 0.5, except for the ZrTi-MAO coating, for which the friction coefficient decreased to 0.3.

The wear rate (Fig. 9b) was determined from the wear track profile (Fig. 8), and the width of the wear track was used as an additional parameter for wear comparison (Fig. 9a). For the Ti-PVD and ZrTi-PVD samples, the measured values were comparable to the values for the Ti-6Al-4V alloy. Both the Ti-PVD coatings and the ZrTi-PVD coatings were abraded to the Ti-6Al-4V base material. This is also confirmed by the analysis of the chemical composition of EDX after tribological tests in PBS presented in Table 6. The chemical composition in the middle of the trace is comparable to the chemical composition of the Ti-6Al-4V base material.

In contrast, a significant decrease in the wear rate was confirmed for the MAO coatings. Only the outer layer (Fig. 8) of the Ti-MAO coating was abraded. This is confirmed in Table 6, where there is a clear decrease in Si in the middle of the friction trace. The amount of Si dropped from 21.0 wt% to 3.8 wt%.

However, the ZrTi-MAO coating clearly showed the best wear resistance properties. The outer layer was minimally abraded at the point of friction (Fig. 8). This is confirmed by a comparison between the chemical composition in the middle of the wear trace and on the outside of the wear trace, which is unchanged (Table 5).

The ZrTi-MAO sample confirmed low friction and very good wear resistance in comparison with the Ti-MAO sample (Fig. 9 and Table 5), and also in comparison with the MAO sample (basic Ti-6Al-4V material modified with MAO), which was tested in our previous work [36].

Because only a small amount of surface wear was detected on the ZrTi-MAO sample, the chemical and bonding composition analysed by XPS can be used to explain this significant difference in

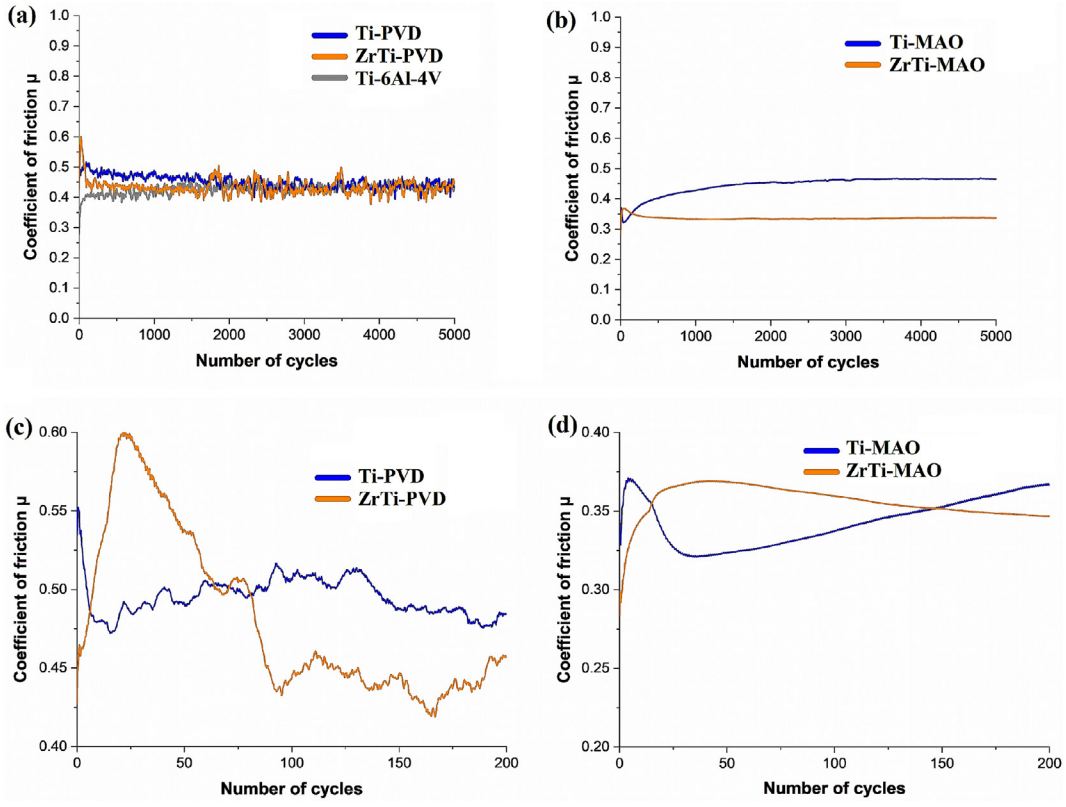

Fig. 7. A comparison of the friction coefficients of the Ti-6Al-4V, Ti-PVD and ZrTi-PVD samples (a), the Ti-MAO and ZrTi-MAO samples (b), and their running-in phases (c, d).

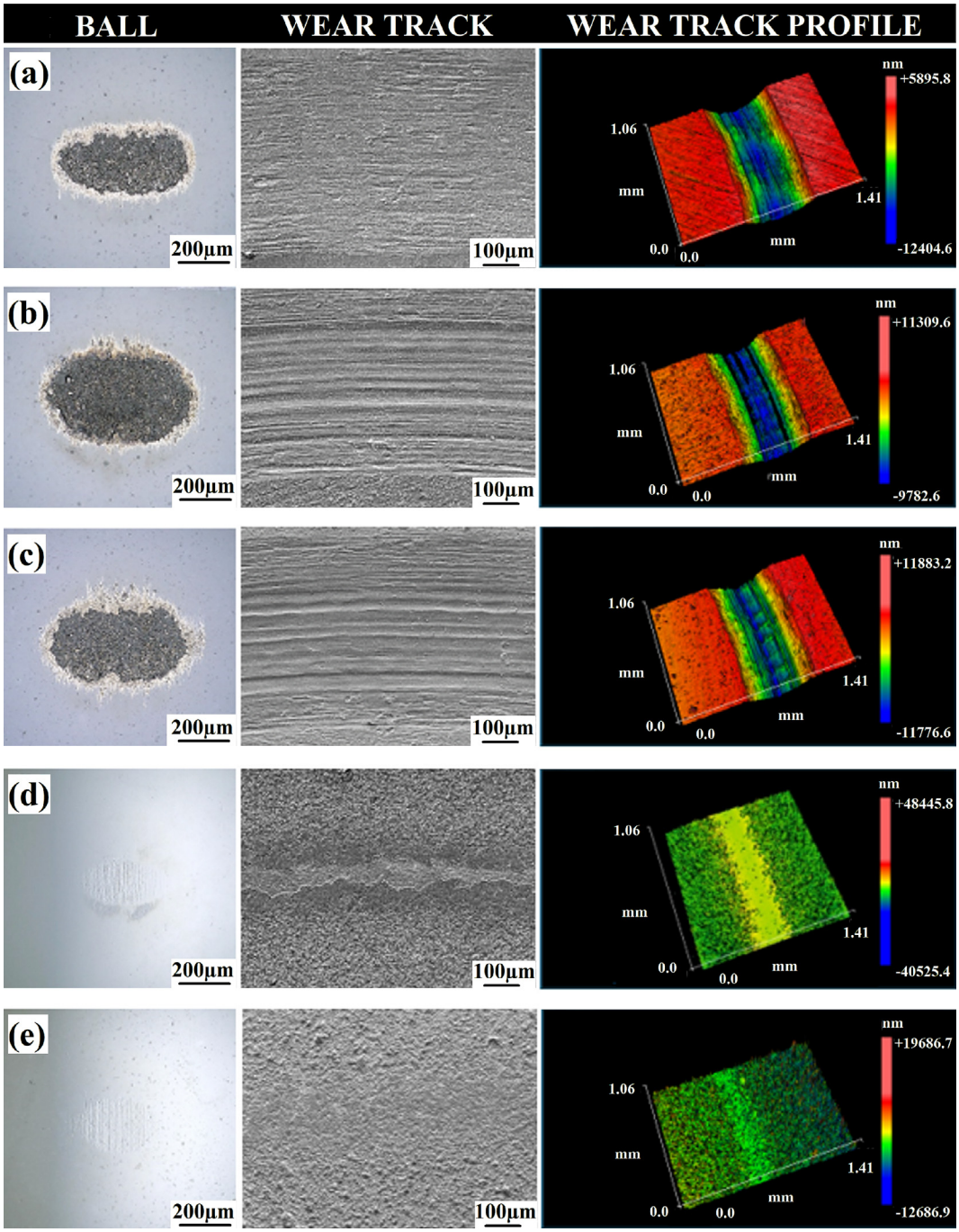

Fig. 8. Al_2O_3 ball wear from an optical microscope (left), the wear track from SEM (middle) and the wear track profile from an optical profilometer (right) for the Ti-6Al-4V (a), Ti-PVD (b), ZrTi-PVD (c), Ti-MAO (d) and ZrTi-MAO (e) samples.

wear. XPS analysis confirmed the occurrence of the a Zr/Si structure, most likely $ZrSi_2$. The presence of a higher amount of $ZrSi_2$ reduces the wear [55] and can lead to the formation of ZrO_x suboxides, which can have the effect of reducing the friction and wear [56]. The combination of a PVD coating with a suitable electrolyte makes it possible to optimize the chemical composition, which has a positive effect on the formation of an abrasion-resistant MAO layer.

The adhesion was evaluated using the scratch test method with a load of 1 N to 30 N. The adhesion between the substrate and PVD coatings was tested before and after MAO treatment (Supplementary Fig. S2). Although MAO coatings based on oxides are brittle, due to the partial porosity and tough interlayer of Ti or TiZr, the cohesion and adhesion of the coating around scratches were not impaired even when a critical force of 30 N was reached. This confirms that hybrid MAO systems have sufficient cohesion and compactness and can be used for the surface treatment of long-term orthopedic implants.

3.3. Corrosion resistance

The impedance spectres were obtained at an amplitude of 10 mV. The tests were always initiated at 100 kHz and were terminated when the sensitivity limit of the testing device was reached

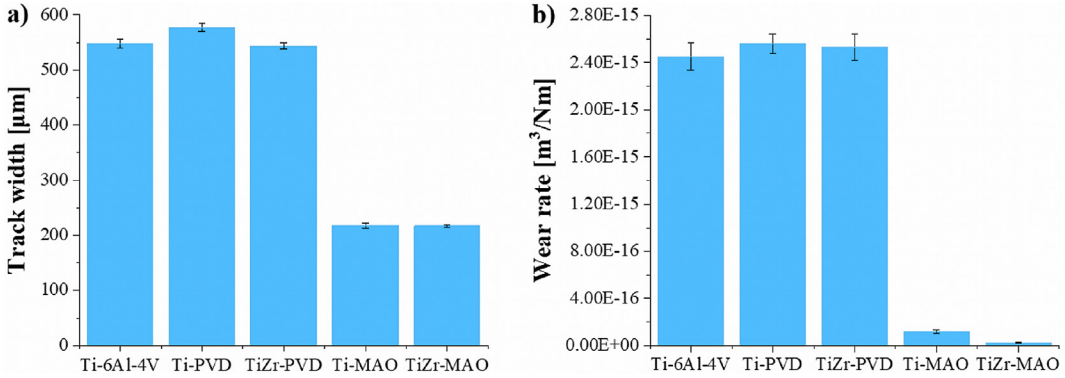

Fig. 9. A comparison of the track widths (a) and the wear rate (b) for samples with a Ti and ZrTi coating (Ti-PVD, ZrTi-PVD), for samples with micro-arc oxidation of the coating (Ti-MAO, ZrTi-MAO), and for the reference Ti-6Al-4V bulk material.

Table 5
EDX analysis of the chemical composition in the middle (*in*) and outside (*out*) parts of the wear trace after tribological tests in PBS.

Element (in wt.%)		Sample				
		Ti-6Al-4V	Ti-PVD	ZrTi-PVD	Ti-MAO	ZrTi-MAO
Ti	in	86.8 ± 0.9	86.2 ± 0.4	86.0 ± 0.4	20.5 ± 1.3	2.9 ± 0.1
	out	85.7 ± 0.2	78.2 ± 0.6	9.9 ± 0.2	8.6 ± 1.1	2.5 ± 0.2
Al	in	10.9 ± 0.8	11.1 ± 0.4	11.1 ± 0.7	0.2 ± 0.1	0.2 ± 0.1
	out	11.4 ± 0.2	0.5 ± 0.2	5.3 ± 0.2	0.3 ± 0.1	–
V	in	2.3 ± 0.1	2.7 ± 0.5	2.6 ± 0.4	–	–
	out	2.9 ± 0.2	–	0.3 ± 0.1	–	–
Si	in	–	–	–	3.1 ± 0.7	5.3 ± 0.1
	out	–	–	–	15.4 ± 0.5	5.1 ± 0.2
Zr	in	–	–	0.2 ± 0.1	–	17.6 ± 0.3
	out	–	–	68.0 ± 2.0	–	18.6 ± 0.2
O	in	–	–	–	76.3 ± 0.6	73.9 ± 0.3
	out	–	21.3 ± 0.7	16.5 ± 2.3	75.7 ± 0.7	73.8 ± 0.2

Table 6
Corrosion parameters of the studied samples obtained by the Tafel method.

Sample	Corrosion potential E_{cor} (mV vs. SCE)	Corrosion rate C_R (µm/year)	Polarisation resistance R_p (kΩ.cm^2)	Corrosion current density J_C (µA/cm^2)
Ti-6Al-4V	−51	0.4	199	0.023
Ti-PVD	28	1.7	110	0.100
Ti-MAO	−8	2.1	174	0.125
ZrTi-PVD	−369	0.2	1310	0.012
ZrTi-MAO	56	1.1	673	0.064

at approx. 0.1–1 Hz due to the high value of the impedance itself. Ten measurements were performed per each frequency decade. The values of the real impedance (Z_r) and the imaginary impedance (Z_i) were obtained for each frequency. These values were later used for calculating the absolute impedance (Z) according to equation (1) and phase shift (θ) according to equation (2) [57].

$$Z = \sqrt{Z_i^2 + Z_r^2} \tag{1}$$

$$\theta = arctg\left(\frac{Z_i}{Z_r}\right) \tag{2}$$

Bode (Fig. 10a), Nyquist (Fig. 10b) and phase shift diagrams (Fig. 10c) were assembled from measured and calculated values. These diagrams truly represent the electrochemical behaviour of the surface layers at varying applied frequencies.

The equivalent circuit was found for each sample with the use of EIS Spectrum Analyser software. Each curve was fitted to the simulated data with relative deviation lower than 2%. The equivalent circuits consisting of resistors (R), capacitors (C), the Warburg element (W) and the constant phase elements (CPE) are shown in Supplementary Fig. S3. Each element of the circuit represents a certain electrochemical property of a complex surface layer.

A polarization curve was recorded during the testing procedure to determine the common corrosion parameters by Tafel extrapolation [58] and by the Stern-Geary method [59]. The test was automatically stopped when the potential value reached 8000 mV vs. SCE, or when the current density reached 5 mA/cm^2. The curves obtained by polarization are illustrated in Fig. 11.

The corrosion parameters (corrosion potential, polarization resistance and corrosion current density) were determined automatically by Voltamaster 10 software by Tafel extrapolation method.The corrosion rate was further calculated from the value of corrosion current density using the Faraday equation [60], where Ti-6Al-4V density of 4.5 g/cm^3 and corroded ions valency of 4 were considered. There was a general corrosion considered for the calculation. The corrosion parameters of the tested samples are summarized and presented in Table 6.

Corrosion pits were found on the surface of samples on which a breakdown of the passive layer occurred during potentiodynamic polarization. This was characterized by a sudden change of the current density. The pits were very shallow and wide open, which

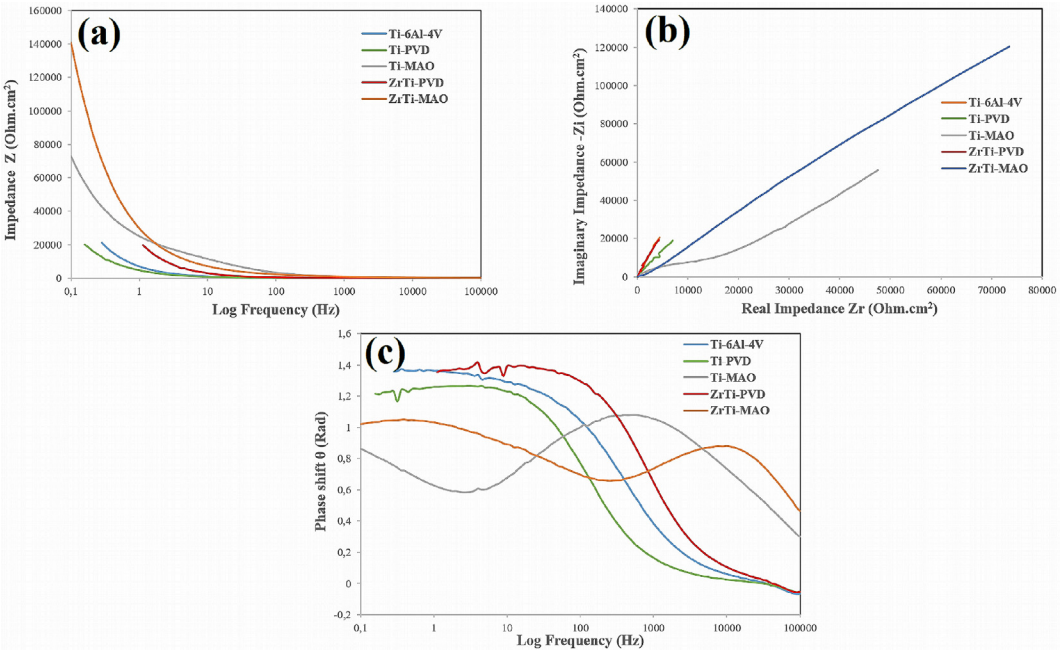

Fig. 10. Bode (a), Nyquist (b) and phase shift (c) diagrams of the studied samples.

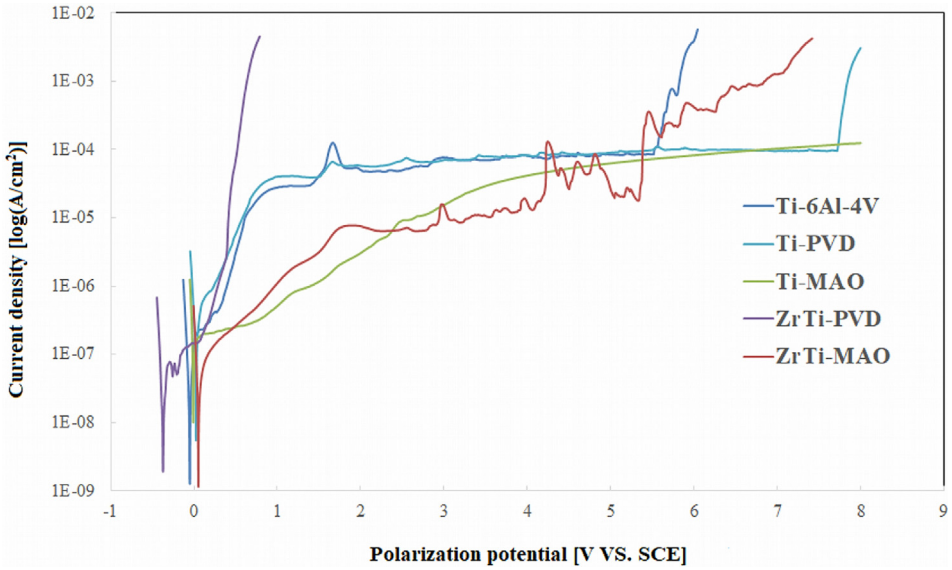

Fig. 11. Polarization curves of studied samples for a 0.9% NaCl solution.

indicates high stability of the substrate material. A representative pit found on the surface of the Ti-PVD sample accompanied by the EDX spectrum of the corrosion products is illustrated in Supplementary Fig. S4. The only sample which remained stable until the maximum device voltage limit was Ti-PVD + MAO. In addition, no corrosion pits were found on the exposed surface.

Three different equivalent circuits were found for different surface states of the tested samples. The number of elements in each circuit increases with the complexity of the surface treatment of the sample. Similar circuits have been proposed by other authors for a passivated titanium surface and for more complicated layers [61,62]. In contrast with these studies, it was found by simulation that in more complicated and partially porous layers, Warburg elements fit the measured spectres better than standard resistors. Warburg elements represent the diffusion coefficient of charged ions across the surface layers. Additionally, on the frequency domain, the spectrum of Warburg element appears at low frequencies (<10 Hz). For this reason, the Warburg impedance is a central key parameter for determining diffusion coefficient values. The curves illustrated in the phase shift diagram also indicate that micro arc oxidation significantly changes the electrochemical properties of the surface layers, as these curves vary considerably from the other curves, especially at lower frequencies and at higher frequencies, where the diffusivity or the conductivity of the surface layers changes the shape of the curves the most. All three diagrams related to EIS measurements suggest that a single PVD surface

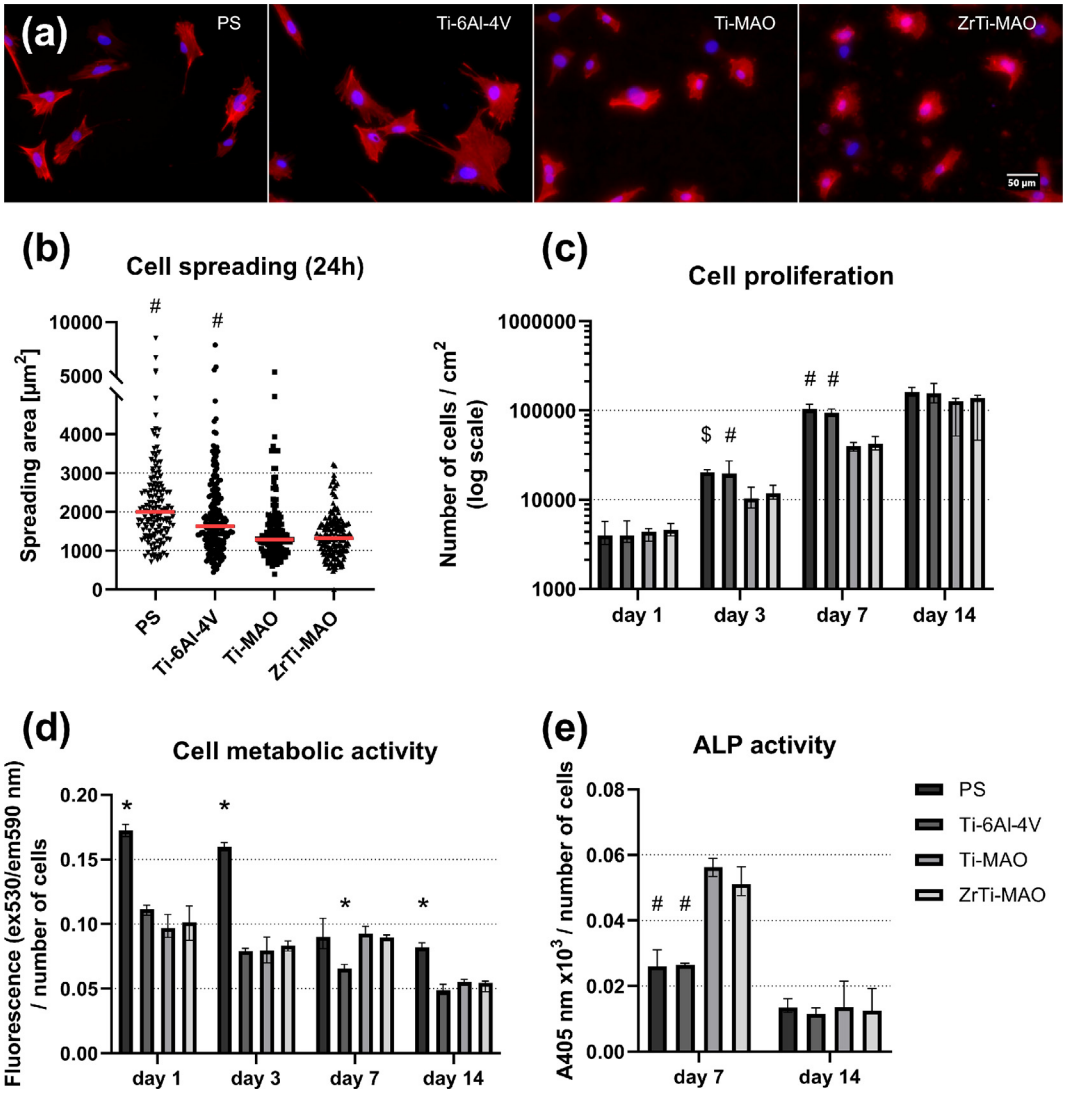

Fig. 12. Assessing the growth and differentiation of hBMSC cells on the materials. Cell morphology (a), cell spreading area (b), cell proliferation (c), metabolic activity of cells growing on the samples (d), and an estimate of the early osteogenic differentiation potential measured by the enzymatic activity of alkaline phosphatase (e). The cells in (a) are stained with phalloidin–TRITC (red fluorescence; F-actin cytoskeleton), and with DAPI (blue fluorescence; nuclei), scale bar = 100 µm. Graph (b) shows single measurements with a median red line. The data in graphs (c, d, e) are expressed as the median with IQR. The data in (d) and (e) were normalized to the number of cells approximated per sample. Statistical significance ($p < 0.05$): $ vs. Ti–MAO; # vs. Ti–MAO, ZrTi–MAO; * vs. all other samples.

treatment changes the character of the surface charge transfer phenomena less significantly than when the material is used in the as-received state.

The corrosion parameters of the as-received sample were comparable with and in accordance with previous studies [63]. In comparison with the as-received state, no significant shift of corrosion potential was found for any sample except ZrTi-PVD, where an almost 300 mV shift to a more negative potential was measured. This may have been due to the more negative standard potential of zirconium, which greatly affects the resulting corrosion potential. On the other hand, the same sample showed the lowest current density and the lowest annual corrosion rate, which indicates improved stability of the spontaneously formed passive layer [64]. However, if the potential is increased to higher values, the untreated layer becomes unstable and even causes a substantial reduction in breakdown potential to values typical for lower grade stainless steels [65]. The highest polarization resistance found for samples with added Zr are in correlation with the EIS method results, i.e. the dielectric properties of zirconium oxides also raise the absolute impedance values. The proposed surface treatment of Ti-MAO and ZrTi-MAO increases the values of the breakdown potential of the tested surface, and according to [66], this treatment can be recommended for application in long-term implant surface coatings.

3.4. Cell adhesion, proliferation and differentiation

The initial adhesion and spreading of mesenchymal stem cells from human bone marrow (hBMSC) showed that both modified samples (Ti-MAO, ZrTi-MAO) supported cell adhesion to a similar extent (Fig. 12a, b). The cells on the modified samples were mostly of compact shape, with a predominantly polygonal morphology and small protrusions, or were spindle-shaped. The cells on samples of untreated Ti-6Al-4V alloy (substrate) and standard polystyrene tissue culture well bottoms (PS, reference) were found to be more spread, more articulated (indented), and with longer protrusions (Fig. 12a). However, the number of adhered cells on day 1 was comparable on all samples. This is typically a result of the immediate interaction of cells with the surface of the sample, which was rougher in the modified samples, in contrast to the

Table 7
Doubling times and cell viability of hBMSC cells in the exponential growth phase. Calculation based on the number of cells growing on the samples on day 1 and on day 3. Data expressed as mean ± SD. Statistical significance ($p < 0.05$): # vs. Ti-MAO, ZrTi-MAO.

Population doubling time D1-D3		Cell viability (%)
Sample	Hours	Day 3
PS	25.40 ± 2.89	99.91 ± 0.26
Ti-6Al-4V	23.17 ± 5.95	99.95 ± 0.20
Ti-MAO	41.28 ± 9.90	98.30 ± 2.33
ZrTi-MAO	39.64 ± 8.97	97.93 ± 1.59

reference Ti-6Al-4V and PS smooth surfaces. The slight increase in cell numbers on ZrTi-MAO in comparison with the Ti-MAO samples which was seen on day 1 (Fig. 12c) can be attributed to an early cell reaction to the higher hydrophilicity of the ZrTi-MAO surface (contact angle 69.01°±5.63° in comparison with 72.32°±4.15° on Ti-MAO). This slight difference is also documented by the calculated cell population doubling time on the Ti-MAO and ZrTi-MAO samples, which were similar to each other (41.3 and 39.6 h, respectively), but these times were significantly slower than on Ti-6Al-4V (23.2 h) and on PS (25.4 h) (Table 7). Slower cell growth on the modified samples was observable from day 3 through the rest of the experiment (Fig. 12c). Since the cells were cultured in the growth medium until day 3 of culture, it can be assumed that the differences in cell proliferation that were initiated between days 1 and 3 were so pronounced that this trend persisted until day 7, and was still observable on day 14, when the cells were cultured in the medium promoting osteogenic differentiation. On day 3, when the differences in the proliferation rate on the samples became more pronounced, the viability of the cells remained very high and was similar for all types of samples (Table 7). These differences should therefore probably be attributed to the distinctive surface morphology and the roughness of the samples, which can hamper the ability of the cells to spread and proliferate without negatively affecting their viability.

Although the adhering hBMSC cells spread easily and proliferated more quickly on the surface of the unmodified samples, the cells on the modified Ti-MAO and ZrTi-MAO samples were more metabolically active than the cells on Ti-6Al-4V, but not on PS, on day 7 (Fig. 12d). However, the cells on the Ti-MAO and ZrTi-MAO samples exhibited greater activity of alkaline phosphatase (ALP; Fig. 12e) than the cells on Ti-6Al-4V and on PS on the same day of culture. Alkaline phosphatase is commonly used as an early or mid-term marker of osteogenic cell differentiation, as it plays an important role during mineralization of the surrounding ECM by bone cells [1,36]. The ALP activity dropped on day 14 in a similar manner in all samples (Fig. 12e). However, there was a notable increase in the metabolic activity (Fig. 12d) but not in the cell proliferation, as indicated by the numbers of cells cultured on PS (Fig. 12c).

The surface parameters - morphology, roughness, stiffness, material composition, chemical functional groups, wettability, surface energy and charge - can profoundly affect the cellular responses. It is widely accepted that these physical and chemical properties have a synergistic effect; however, this complexity also means that the effects, taken together, are not easy to assess, nor is there a clear consensus on their ideal values for specific materials, for a specific purpose and for a selected *in vitro* model [67]. Surface texture properties, such as pore size, volume and structure, can significantly affect the bone-to-implant contact [68]. It has been confirmed in Ti-6Al-4V alloy that surfaces with micron-scale roughness, and especially hierarchically-organised multiscale surfaces of implants with a combination of micron- and nano-scale irregularities, achieve better contact and anchorage with the bone than mechanically machined implant surfaces [69]. Hierarchically-organised surfaces imitate the architecture of the native bone tissue and provide structural cues for osteoblasts and mesenchymal stem cells to stimulate osteogenesis [70,71]. In addition, these surfaces, developed on Ti-6Al-4V alloy by femtosecond laser treatment combined with sandblasting, showed anti-inflammatory properties, as documented by the polarization of macrophages towards M2 phenotype, characterized by increased secretion of anti-inflammatory factors and decreased production of pro-inflammatory factors [71].

However, it should be taken into account that increased micron-scale surface roughness can hamper cell spreading, proliferation and proteosynthesis, including the synthesis of collagen, an important component of the bone matrix. It can therefore limit the creation of sufficient bone mass for osseointegration of the implant [1,36]. The surface topography, together with the presence of various chemical functional groups on the surface of a biomaterial, affects the resulting surface charge and wettability (hydrophobicity/hydrophilicity). These factors influence the early cell adhesion, further proliferation and differentiation by affecting the conformation of the proteins adsorbed at the surface of the material from the cultivation media *in vitro* or from the physiological fluids *in vivo*, the amount of adsorbed proteins, and the strength of their adsorption bonds [68,72]. Proteins on highly hydrophobic surfaces with low surface energy lose their natural conformation and are bonded with an altered conformation of the integrin domain binding receptors. Very hydrophilic surfaces, on the other hand, provide weak binding, and cell adhesion can be more or less impaired, or even prevented [36]. Considerably better conditions are reported to be provided on slightly hydrophilic surfaces, which can boost cell adhesion and promote the cell function [70,71]. The influence of these factors was also observed in our data. The combined effect of the porous structure, with an average pore size of 1 μm, and the rugged morphology of the MAO-treated samples, slowed the initial cell spreading and proliferation in comparison with a rather smooth Ti-6Al-4V substrate material and PS. The positive effect of the slight hydrophilicity of the MAO-treated samples was observable in the numbers of adhered cells on day 1, which were comparable or even slightly higher than on the substrate material and on the PS control. Of the two types of MAO-treated samples, ZrTi-MAO, which is more hydrophilic and less rough (in terms of Rz), exhibited more favorable surface properties for cell proliferation. However, the less hydrophilic and rougher surface of Ti-MAO was better for promoting early osteogenic differentiation of the cells. Similar results were obtained with MG-63 cells cultured on MAO-treated Ti substrates [73]. In that study, the samples modified with porous Ti-Zr oxide films performed better than the samples without Zr in cell proliferation and differentiation, as indicated by higher expression of ALP and other osteogenic genes. Zr-coating of Ti-6Al-4V alloy by magnetron sputtering also resulted in good adhesion, enhanced proliferation, higher ALP activity and expression of early osteogenic markers by MC3T3-E1 mouse pre-osteoblast cells [74]. In addition, Zr had a positive effect on the cell and material performance not only as a component of coating, but also as a component of bulk material. In a recent study, a Ti-Nb-Ta-Zr-O alloy showed lower corrosion rate and improved attachment of MC3T3-E1 pre-osteoblasts than the alloy without Zr, i.e. Ti-Nb-Ta-O alloy [75].

4. Conclusions

The results of our preliminary study have confirmed the high potential of the newly-developed hybrid layers for surface modification of orthopaedic implants. The hydrophilic oxide structure of the MAO coatings was prepared using cathodic arc evaporation and MAO technology. The Ti and ZrTi oxide layers were doped with C

and Si ions from the electrolyte to optimize the chemical composition in terms of corrosion resistance, tribological and biological properties. Application of the EIS non-destructive technique confirmed that both types of coatings (Ti-MAO, ZrTi-MAO) increase the corrosion resistance of the Ti-6Al-4V alloy. Furthermore, the Ti / Si component (mainly in the form of $ZrSi_2$) significantly affected both the friction and the wear of the hybrid ZrTi-MAO coating. It reduced the wear rate more than tenfold and, at the same time, reduced the coefficient of friction from 0.5 to 0.3 compared to the Ti-MAO and MAO coatings. Our results also indicate that both types of sample modifications can stimulate osteogenic differentiation better than the unmodified alloy, i.e. the cells on these samples proliferated more slowly but started to differentiate at an earlier time point, which is documented by increased ALP enzyme activity. Hybrid surface modification of the Ti-6Al-4V alloy proved the possibility of purposefully modifying the surface without the presence of undesirable elements (Al, V) in the surface layer and, at the same time, confirmed that there was an increase in biocompatibility, wear resistance and corrosion resistance. At the same time, the hybrid coatings show very good adhesion and cohesiveness. For these reasons, this combination of methods seems to be a suitable tool for preparing functional layers on other types of materials used in orthopaedic bone implants.

Declaration of Competing Interest

The authors declare that they have no known competing financial interests or personal relationships that could have appeared to influence the work reported in this paper.

Acknowledgments

This study was conducted with financial support from the Technology Agency of the Czech Republic (TACR; PRE SEED fund II VSB – Technical University of Ostrava [grant No. TP01010036]); and from the Grant Agency of the Czech Republic [grant No. 20-01570S]. Mr. Robin Healey (Czech Technical University in Prague) is gratefully acknowledged for the language revision of the manuscript.

Authors' contributions

R.G.: Conceptualization, Methodology, Investigation, Formal Analysis, Visualization, Project administration, Writing – Original Draft, Funding Acquisition. L.C.: Methodology, Investigation, Formal Analysis, Visualization, Writing – Original Draft. M.D.: Conceptualization, Methodology, Investigation, Formal Analysis, Visualization, Validation, Writing – Original Draft. V.N.: Methodology, Investigation, Formal Analysis, Visualization, Writing – Original Draft, Funding Acquisition. J.H.: Methodology, Investigation, Formal Analysis, Visualization, Writing – Original Draft, Funding Acquisition. S.C.: Methodology, Investigation. P.U.: Methodology, Investigation M.B.: Methodology, Investigation. A.P.: Methodology, Investigation. J.S.: Supervision, Writing – Review & Editing. L.B.: Supervision, Writing – Review & Editing, Funding Acquisition.

Appendix A. Supplementary material

Supplementary data to this article can be found online at https://doi.org/10.1016/j.matdes.2022.110811.

References

[1] M. Vandrovcova, Z. Tolde, P. Vanek, V. Nehasil, M. Doubková, M. Trávníčková, J. Drahokoupil, E. Buixaderas, F. Borodavka, J. Novakova, L. Bacakova, Beta-titanium alloy covered by ferroelectric coating-physicochemical properties and human osteoblast-like cell response, Coatings 11 (2) (2021) 210.
[2] M. Geetha, A.K. Singh, R. Asokamani, A.K. Gogia, Ti based biomaterials, the ultimate choice for orthopaedic implants – a review, Prog. Mater Sci. 54 (2009) 397–425, https://doi.org/10.1016/j.pmatsci.2008.06.004.
[3] F. H. Froes, Titanium: Physical Metallurgy, Processing, and Applications, ASM International, 2015. ISBN-13: 978-1-62708-079-8.
[4] N. Mavros, T. Larimian, J. Esqivel, R.K. Gupta, R. Contieri, T. Borkar, Spark plasma sintering of low modulus titanium-niobium-tantalum-zirconium (TNTZ) alloy for biomedical applications, Mater. Des. 183 (2019), https://doi.org/10.1016/j.matdes.2019.108163 108163.
[5] S. Karimi, T. Nickchi, A. Alfantazi, Effects of bovine serum albumin on the corrosion behaviour of AISI 316L, Co–28Cr–6Mo, and Ti–6Al–4V alloys in phosphate buffered saline solutions, Corros. Sci. 53 (2011) 3262–3272, https://doi.org/10.1016/j.corsci.2011.06.009.
[6] R. Messous, B. Henriques, H. Bousbaa, F.S. Silva, W. Teughels, J.C.M. Souza, Cytotoxic effects of submicron- and nano-scale titanium debris released from dental implants: an integrative review, Clin Oral Investig. 25 (2021) 1627–1640, https://doi.org/10.1007/s00784-021-03785-z.
[7] P. Jiang, X.L. He, X.X. Li, L.G. Yu, H.M. Wang, Wear resistance of a laser surface alloyed Ti–6Al–4V alloy, Surf. Coat. Technol. 130 (1) (2000) 24–28.
[8] D. Du, D. Liu, Z. Ye, X. Zhang, F. Li, Z. Zhou, L. Yu, Fretting wear and fretting fatigue behaviors of diamond-like carbon and graphite-like carbon films deposited on Ti-6Al-4V alloy, Appl. Surf. Sci. 313 (2014) 462–469, https://doi.org/10.1016/j.apsusc.2014.06.006.
[9] Z.K. Chang, X.S. Wan, Z.L. Pei, J. Gong, C. Sun, Microstructure and mechanical properties of CrN coating deposited by arc ion plating on Ti6Al4V substrate, Surf. Coat. Technol. 205 (19) (2011) 4690–4696.
[10] Y. Wang, H. Yu, C. Chen, Z. Zhao, Review of the biocompatibility of micro-arc oxidation coated titanium alloys, Mater. Des. 85 (2015) 640–652, https://doi.org/10.1016/j.matdes.2015.07.086.
[11] K.A. Kravanja, M. Finšgar, A review of techniques for the application of bioactive coatings on metal-based implants to achieve controlled release of active ingredients, Mater. Des. 217 (2022), https://doi.org/10.1016/j.matdes.2022.110653 110653.
[12] J. Lin, D.W.D. Sproul, J.J. Moore, Tribological behavior of thick CrN coatings deposited by modulated pulsed power magnetron sputtering, Surf. Coat. Technol. 206 (2012) 2474–2483, https://doi.org/10.1016/j.surfcoat.2011.10.053.
[13] Y. Deng, W. Chen, B. Li, C.h. Wang, T. Kuang, Y. Li, Physical vapor deposition technology for coated cutting tools: A review, Ceram Internat. 46 (2020) 18373–18390, https://doi.org/10.1016/j.ceramint.2020.04.168.
[14] U. Helmersson, M. Lattemann, J. Bohlmark, A.P. Ehiasarian, J.T. Gudmundsson, Ionized physical vapor deposition (IPVD): A review of technology and applications, Thin Solid Films 513 (2006) 1–24, https://doi.org/10.1016/j.tsf.2006.03.033.
[15] V. Stranak, S. Drache, R. Bogdanowicz, H. Wulff, A.P. Herrendorf, Z. Hubicka, M. Cada, M. Tichy, R. Hippler, Effect of mid-frequency discharge assistance on dual-high power impulse magnetron sputtering, Surf. Coat. Technol. 206 (2012) 2801–2809, https://doi.org/10.1016/j.surfcoat.2011.11.043.
[16] A. Anders, A review comparing cathodic arcs and high power impulse magnetron sputtering (HiPIMS), Surf. Coat. Technol. 257 (2014) 308–325, https://doi.org/10.1016/j.surfcoat.2014.08.043.
[17] T.H. Teh, A. Berkani, S. Mato, P. Skeldon, G.E. Thompson, H. Habazaki, K. Shimizu, Initial stages of plasma electrolytic oxidation of titanium, Corros. Sci. 45 (2003) 2757–2768, https://doi.org/10.1016/S0010-938X(03)00101-X.
[18] Y.M. Wang, B.L. Jiang, T.Q. Lei, L.X. Guo, Microarc oxidation coatings formed on Ti6Al4V in Na_2SiO_3 system solution: Microstructure, mechanical and tribological properties, Surf. Coat. Technol. 201 (2006) 82–89, https://doi.org/10.1016/j.surfcoat.2005.10.044.
[19] R.G. Santos-Coquillat, M. Tenorio, E. Mohedano, R. Martinez-Campos, E.M. Arrabal, Tailoring of antibacterial and osteogenic properties of Ti6Al4V by plasma electrolytic oxidation, Appl. Surf. Sci. 454 (2018) 157–172, https://doi.org/10.1016/j.apsusc.2018.04.267.
[20] X.L. Zhang, Z.H. Jiang, Z.P. Yao, Z.D. Wu, Electrochemical study of growth behaviour of plasma electrolytic oxidation coating on Ti6Al4V: Effects of the additive, Corr Sci. 52 (2010) 3465–3473, https://doi.org/10.1016/j.corsci.2010.06.017.
[21] G. Rapheal, S. Kumar, C. Blawert, N.B. Dahotre, Wear behavior of plasma electrolytic oxidation (PEO) and hybrid coatings of PEO and laser on MRI 230D magnesium alloy, Wear 271 (2011) 1987–1997, https://doi.org/10.1016/j.wear.2010.12.013.
[22] H.R. Bakhsheshi-Rad, E. Hamzah, A.F. Ismail, M. Aziz, M. Daroonparvar, E. Saebnoori, A. Chami, In vitro degradation behavior, antibacterial activity and cytotoxicity of TiO2-MAO/ZnHA composite coating on Mg alloy for orthopedic implants, Surf. Coat. Technol. 334 (2018) 450–460, https://doi.org/10.1016/j.surfcoat.2017.11.027.
[23] B.S. Lou, J.W. Lee, C.M. Tseng, Y.Y. Lin, C.A. Yen, Mechanical property and corrosion resistance evaluation of AZ31 magnesium alloys by plasma electrolytic oxidation treatment: Effect of MoS_2 particle addition, Surf. Coat. Technol. 350 (2018) 813–822, https://doi.org/10.1016/j.surfcoat.2018.04.044.
[24] K.M. Lee, K.R. Shin, S. Namgung, B. Yoo, D.H. Shin, Electrochemical response of ZrO_2-incorporated oxide layer on AZ91 Mg alloy processed by plasma electrolytic oxidation, Surf. Coat. Technol. 205 (2011) 3779–3784, https://doi.org/10.1016/j.surfcoat.2011.01.033.

[25] B. Zhang, B. Li, S. Gao, Y. Li, R. Cao, J. Cheng, R. Li, E. Wang, Y. Guo, K. Zhang, J. Liang, B. Liu, Y-doped TiO_2 coating with superior bioactivity and antibacterial property prepared via plasma electrolytic oxidation, Mater. Des. 192 (2020), https://doi.org/10.1016/j.matdes.2020.108758 108758.

[26] M.J. Mazinani, R. Nine, G. Chiesa, P. Candiani, T.T. Tarsini, D. Tung, Losic, **Graphene oxide (GO) decorated on multi-structured porous titania fabricated by plasma electrolytic oxidation (PEO) for enhanced antibacterial performance**, Mater. Des. 200 (2021), https://doi.org/10.1016/j.matdes.2020.109443 109443.

[27] S.H. Kang, W.B. Tu, J.X. Han, Z. Li, Y.L. Cheng, A significant improvement of the wear resistance of Ti6Al4V alloy by a combined method of magnetron sputtering and plasma electrolytic oxidation (PEO), Surf. Coat. Technol. 358 (2019) 879–890, https://doi.org/10.1016/j.surfcoat.2018.12.025.

[28] A. Kozelskaya, G. Dubinenko, A. Vorobyev, A. Fedotkin, N. Korotchenko, A. Gigilev, E. Shesterikov, Y. Zhukov, S. Tverdokhlebov, Porous CaP coatings formed by combination of plasma electrolytic oxidation and rf-magnetron sputtering, Coatings 10 (11) (2020) 1113.

[29] S. Y. Park, H. Ch. Choe, **Mn-coatings on the micro-pore formed Ti-29Nb-xHf alloys by RF-magnetron sputtering for dental applications,** Appl Surf Sci., 432 (2018), pp. 432:278-284. DOI.org/10.1016/j.apsusc.2017.08.023.

[30] J. Hwang, H.C. Choe, Surface morphology and cell behavior of Zn-coated Ti-6Al-4V alloy by RF-sputtering after PEO-treatment, Surf. Coat. Technol. 361 (2019) 386–395, https://doi.org/10.1016/j.surfcoat.2019.01.061.

[31] Y.L. Zhou, M. Niinomi, T. Akahori, H. Fukui, H. Toda, Corrosion resistance and biocompatibility of Ti–Ta alloys for biomedical applications, Mater. Sci. Eng., A 398 (2005) 28–36, https://doi.org/10.1016/j.msea.2005.03.032.

[32] C. Wang, F. Ma, P. Liu, J. Chen, X. Liu, K.e. Zhang, W. Li, Q. Han, The influence of alloy elements in Ti6Al4V and Ti35Nb2Ta3Zr on the structure, morphology and properties of MAO coatings, Vacuum 157 (2018) 229–236, https://doi.org/10.1016/j.vacuum.2018.08.054.

[33] S.L. Aktug, I. Kutbay, M. Usta, Characterization and formation of bioactive hydroxyapatite coating on commercially pure zirconium by micro arc oxidation, J. Alloy. Compd. 695 (2017) 998–1004, https://doi.org/10.1016/j.jallcom.2016.10.217.

[34] Y. Yan, Y. Han, D. Li, J. Huang, Q. Lian, Effect of $NaAlO_2$ concentrations on microstructure and corrosion resistance of Al_2O_3/Zr_2O_3 coatings formed on zirconium by micro-arc oxidation, Appl. Surf. Sci. 256 (2010) 6359–6366, https://doi.org/10.1016/j.apsusc.2010.04.017.

[35] L. Wang, X. Hu, X. Nie, Deposition and properties of zirconia coatings on a zirconium alloy produced by pulsed DC plasma electrolytic oxidation, Surf. Coat. Technol. 221 (2013) 150–157, https://doi.org/10.1016/j.surfcoat.2013.01.040.

[36] R. Gabor, M. Doubkova, S. Gorosova, K. Malanik, M. Vandrovcova, L. Cvrcek, K. Drobikova, K. Mamulova Kutlakova, L. Bacakova, Preparation of highly wettable coatings on Ti–6Al–4V ELI alloy for traumatological implants using micro-arc oxidation in an alkaline electrolyte, Sci. Rep. 10 (2020) 19780, https://doi.org/10.1038/s41598-020-76448-w.

[37] S.N. Rosenbloom, R.A. Corbett, An assessment of ASTM F 2129 test results comparing nitinol to other implant alloys, **In Proceedings of the SMST-2006,** Proceedings of the International Conference on Shape Memory and Superelastic Technologies (ASM International), 2008.

[38] G.Y. Du, D.C. Ba, Z. Tan, W. Sun, K. Liu, Q.K. Han, Vibration damping performance of ZrTiN coating deposited by arc ion plating on TC4 Titanium alloy, Surf. Coat. Technol. 229 (2013) 172–175, https://doi.org/10.1016/j.surfcoat.2012.05.140.

[39] R. Gabor, L. Cvrček, S. Causidu, K. Drobíková, M. Večeř, K.M. Kutláková, M. Buřil, J. Hlinka, J. Seidlerová, Effect of additive for preparation of reduced-porosity ceramic layer on Ti-6Al-4V alloy for orthopaedic and trauma implants, Surf. Interfaces 25 (2021), https://doi.org/10.1016/j.surfin.2021.101209 101209.

[40] Y. Cheng, F. Wu, E. Matykina, P. Skeldon, G.E. Thompson, The influences of microdischarge types and silicate on the morphologies and phase compositions of plasma electrolytic oxidation coatings on Zircaloy-2, Corros. Sci. 59 (2012) 307–315, https://doi.org/10.1016/j.corsci.2012.03.017.

[41] R. Wang, X. He, Y. Gao, X. Zhang, X. Yao, B. Tang, Antimicrobial property, cytocompatibility and corrosion resistance of Zn-doped ZrO_2/TiO_2 coatings on Ti6Al4V implants, Mater. Sci. Eng., C 75 (2017) 7–15, https://doi.org/10.1016/j.msec.2017.02.036.

[42] Y.C. Jung, K.R.Shin, Y.G.Ko, D.H. Shin, Surface characteristics and biological response of titanium oxide layer formed via micro-arc oxidation in K3PO4 and Na3PO4 electrolytes, J. Alloys Compd., 586 (2014), pp. S549-S552. DOI.org/10.1016/j.jallcom.2013.01.060.

[43] S. Durdu, M. Usta, A.S. Berkem, Bioactive coatings on Ti6Al4V alloy formed by plasma electrolytic oxidation, Surf. Coat. Technol. 301 (2016) 85–93, https://doi.org/10.1016/j.surfcoat.2015.07.053.

[44] J.M. Ríos, D. Quintero, J.G. Castaňa, F. Echeverría, M.A. Gómez, Comparison among the lubricated and unlubricated tribological behaviour of coatings obtained by PEO on the Ti6Al4V alloy in alkaline solutions, Tribol. Int. 128 (2018) 1–8, https://doi.org/10.1016/j.triboint.2018.07.010.

[45] E. Matykina, R. Arrabal, P. Skeldon, G.E. Thompson, P. Wang, P. Wood, Plasma electrolytic oxidation of a zirconium alloy under AC conditions, Surf. Coat. Technol. 204 (2010) 2142–2151, https://doi.org/10.1016/j.surfcoat.2009.11.042.

[46] F. Jaspard-Mécuson, T. Czerwiec, G. Henrion, T. Belmonte, L. Dujardin, A. Viola, J. Beauvir, Tailored aluminium oxide layers by bipolar current adjustment in the Plasma Electrolytic Oxidation (PEO) process, Surf. Coat. Technol. 201 (2007) 8677, https://doi.org/10.1016/j.surfcoat.2006.09.005.

[47] E. Matykina, R. Arrabal, P. Skeldon, G.E. Thompson, Investigation of the growth processes of coatings formed by AC plasma electrolytic oxidation of aluminium, Electrochim. Acta 54 (2009) 6767–6778, https://doi.org/10.1016/j.electacta.2009.06.088.

[48] Y.Y. Wang, K. Kusumoto, C.J. Li, XPS analysis of SiC films prepared by radio frequency plasma sputtering, Phys Procedia 32 (2012) 95–102, https://doi.org/10.1016/j.phpro.2012.03.524.

[49] Y. Wang, J. Lou, L. Zeng, J. Xiang, S. Zhang, J. Wang, F. Xiong, C.h. Li, Y. Zhao, R. Zhang, Osteogenic potential of a novel microarc oxidized coating formed on Ti6Al4V alloys, Appl. Surf. Sci. 412 (2017) 29–36, https://doi.org/10.1016/j.apsusc.2017.03.191.

[50] J. Ding, Z. Huang, Y. Qin, M. Shi, C.h. Huang, J. Mao, Improved ablation resistance of carbon-phenolic composites by introducing zirconium silicide particles, Compos. B Eng. 82 (2015) 100–107, https://doi.org/10.1016/j.compositesb.2015.08.023.

[51] Handbook of Photoelectron Spectroscopy, Edited by Jill Chastain, Perkin-Elmer Corporation, Minesota, USA, 1992.

[52] V.V. Atuchin, V.G. Kesler, N.V. Pervukhina, Z. Zhang, Ti 2p and O 1s core levels and chemical bonding in titanium-bearing oxides, J Electron Spectros Relat Phenomena 152 (2006) 18–24, https://doi.org/10.1016/j.elspec.2006.02.004.

[53] B.M. Reddy, B. Chowdhury, P.G. Smirniotis, An XPS study of the dispersion of MoO_3 on TiO_2–ZrO_2, TiO_2–SiO_2, TiO_2–Al_2O_3, SiO_2–ZrO_2, and SiO_2–TiO_2–ZrO_2 mixed oxides, Appl Catal A Gen 211 (2001) 19–30, https://doi.org/10.1016/S0926-860X(00)00834-6.

[54] K. Wang, D. Xiong, Construction of lubricant composite coating on Ti6Al4V alloy using micro-arc oxidation and grafting hydrophilic polymer, Mater. Sci. Eng., C 90 (2018) 219–226, https://doi.org/10.1016/j.msec.2018.04.057.

[55] J. Song, Z. Huang, Y. Qin, H. Wang, M. Shi, Effects of zirconium silicide on the vulcanization, mechanical and ablation resistance properties of ceramifiable silicone rubber composites, Polymers 12 (2020), https://doi.org/10.3390/polym12020496.

[56] J. Li, X. He, G. Zhang, R. Hang, X. Huang, B. Tang, X. Zhang, Electrochemical corrosion, wear and cell behavior of ZrO_2/TiO_2 alloyed layer on Ti-6Al-4V, Bioelectrochemistry 121 (2018) 105–114, https://doi.org/10.1016/j.bioelechem.2018.01.011.

[57] M. Itagaki, S. Suzuki, I. Shitanda, K. Watanabe, Electrochemical impedance and complex capacitance to interpret electrochemical capacitor, Electrochemistry 75 (2007) 649–655, https://doi.org/10.5796/electrochemistry.75.649.

[58] T.K. Yeh, P.I. Wu, C.H. Tsai, Corrosion of ZrO_2 treated type 304 stainless steels in high temperature pure water with various amounts of hydrogen peroxide, Prog. Nucl. Energy 57 (2012) 62–70, https://doi.org/10.1016/j.pnucene.2011.12.014.

[59] U. Angst, M. Büchler, On the applicability of the Stern-Geary relationship to determine instantaneous corrosion rates in macro-cell corrosion, Mater. Corros. 27 (2014), https://doi.org/10.1002/maco.201407997.

[60] S. Papavinasam, in: Trends in Oil and Gas Corrosion Research and Technologies, Elsevier, 2017, pp. 663–688.

[61] W.Q. Yu, J. Qiu, F.Q. Zhang, In vitro corrosion study of different TiO_2 nanotube layers on titanium in solution with serum proteins, Colloids Surf. B: Biointerfaces 84 (2011) 400–405, https://doi.org/10.1016/j.colsurfb.2011.01.033.

[62] Q. Zhang, M. Zheng, Y. Huang, H.J. Kunte, X. Wang, Y. Liu, C. Zheng, Long term corrosion estimation of carbon steel, titanium and its alloy in backfill material of compacted bentonite for nuclear waste repository, Sci. Rep. 9 (2019), https://doi.org/10.1038/s41598-019-39751-9.

[63] F.E.T. Heakal, K.A. Awad, Electrochemical corrosion and passivation behavior of titanium and its Ti-6AL-4V alloy in low and highly concentrated HBr solutions, Int. J. Electrochem. Sci. 6 (2011) 6483–6502.

[64] A. Yilmazbayhan, A.T. Motta, R.J. Comstock, G.P. Sabol, B. Lai, Z. Cai, Structure of zirconium alloy oxides formed in pure water studied with synchrotron radiation and optical microscopy: Relation to corrosion rate, J. Nucl. Mater. 324 (1) (2004) 6–22.

[65] E. Mujanović, B. Zajec, T. Kosec, A. Legat, S. Hönig, G. Zehethofer, G. Mori, Activation and repassivation of stainless steels in artificial brines as a function of pH, Materials 12 (2019) 3811, https://doi.org/10.3390/ma12233811.

[66] S.N. Rosenbloom, R.A. Corbett, An Assessment of Astm F 2129 Electrochemical Testing of Small Medical Implants - Lessons Learned, Corros. Conf. Expo (CORROSION 2007) 2007, pp. 105–114.

[67] M. Rahmati, E.A. Silva, J.E. Reseland, C.A. Heyward, H.J. Haugen, Biological responses to physicochemical properties of biomaterial surface, Chem. Soc. Rev. 49 (2020) 5178–5224, https://doi.org/10.1039/D0CS00103A.

[68] Z. Wang, M. Zhang, Z. Liu, Y. Wang, W. Dong, S. Zhao, D. Sun, Biomimetic design strategy of complex porous structure based on 3D printing Ti-6Al-4V scaffolds for enhanced osseointegration, Mater. Des. 218 (2022), https://doi.org/10.1016/j.matdes.2022.110721 110721.

[69] W. Zhang, G. Wang, Y. Liu, X. Zhao, D. Zou, C.h. Zhu, Y. Jin, Q. Huang, J. Sun, X. Liu, X. Jiang, H. Zreiqat, The synergistic effect of hierarchical micro/nano-topography and bioactive ions for enhanced osseointegration, Biomaterials 34 (2013) 3184–3195, https://doi.org/10.1016/j.biomaterials.2013.01.008.

[70] X. Li, M. Liu, F. Chen, Y. Wang, M. Wang, X. Chen, Y. Xiao, X. Zhang, Design of hydroxyapatite bioceramics with micro-/nano-topographies to regulate the osteogenic activities of bone morphogenetic protein-2 and bone marrow stromal cells, Nanoscale 12 (2020) 7284–7300, https://doi.org/10.1039/C9NR10561A.

[71] Y. Liu, Z. Rui, W. Cheng, L. Song, Y. Xu, R. Li, X. Zhang, Characterization and evaluation of a femtosecond laser-induced osseointegration and an anti-

inflammatory structure generated on a titanium alloy, Regen Biomater. 8 (2021) rbab006, https://doi.org/10.1093/rb/rbab006.
[72] J. Barberi, S. Ferraris, A.M. Giovannozzi, L. Mandrile, E. Piatti, A.M. Rossi, S. Spriano, Advanced characterization of albumin adsorption on a chemically treated surface for osseointegration: An innovative experimental approach, Mater. Des. 218 (2022), https://doi.org/10.1016/j.matdes.2022.110712 110712.
[73] M.T. Tsai, Y.Y. Chang, H.L. Huang, Y.H. Wu, T.M. Shieh, Micro-arc oxidation treatment enhanced the biological performance of human osteosarcoma cell line and human skin fibroblasts cultured on titanium–zirconium films, Surf. Coat. Technol. 303 (2016) 268–276, https://doi.org/10.1016/j.surfcoat.2016.03.001.
[74] B.A. Lee, H.J. Kim, Y.Z. Xuan, Y.J. Park, H.J. Chung, Y.J. Kim, Osteoblastic behavior to zirconium coating on Ti-6Al-4V alloy, J Adv Prosthodont 6 (2014) 512–520, https://doi.org/10.4047/jap.2014.6.6.512.
[75] S. Acharya, A.G. Panicker, D.V. Laxmi, S. Suwas, K. Chatterjee, Study of the influence of Zr on the mechanical properties and functional response of Ti-Nb-Ta-Zr-O alloy for orthopedic applications, Mater. Des. 164 (2019), https://doi.org/10.1016/j.matdes.2018.107555 107555.